Shahbandeh, M, Hsiao, EY, Ashall, C, Teffs, J, Hoeflich, P, Morrell, N, Phillips, MM, Anderson, JP, Baron, E, Burns, CR, Contreras, C, Davis, S, Diamond, TR, Folatelli, G, Galbany, L, Gall, C, Hachinger, S, Holmbo, S, Karamehmetoglu, E, Kasliwal, MM, Kirshner, RP, Krisciunas, K, Kumar, S, Lu, J, Marion, GH, Mazzali, PA, Piro, AL, Sand, DJ, Stritzinger, MD, Suntzeff, NB, Taddia, F and Uddin, SA

Carnegie Supernova Project-II: Near-infrared Spectroscopy of Stripped-envelope Core-collapse Supernovae*

The Astrophysical Journal, 925:175 (24pp), 2022 February 1 https://doi.org/10.3847/1538-4357/ac4030

Carnegie Supernova Project-II: Near-infrared Spectroscopy of Stripped-envelope Core-collapse Supernovae*

M. Shahbandeh[1], E. Y. Hsiao[1], C. Ashall[2], J. Teffs[3], P. Hoeflich[1], N. Morrell[4], M. M. Phillips[4], J. P. Anderson[5], E. Baron[6], C. R. Burns[7], C. Contreras[4], S. Davis[8], T. R. Diamond[9], G. Folatelli[10], L. Galbany[11], C. Gall[12], S. Hachinger[13], S. Holmbo[14], E. Karamehmetoglu[14], M. M. Kasliwal[15], R. P. Kirshner[16,17], K. Krisciunas[18], S. Kumar[1], J. Lu[1], G. H. Marion[19], P. A. Mazzali[3,20], A. L. Piro[7], D. J. Sand[21], M. D. Stritzinger[14], N. B. Suntzeff[18], F. Taddia[14], and S. A. Uddin[18]

[1] Department of Physics, Florida State University, 77 Chieftan Way, Tallahassee, FL 32306, USA; melissa.shahbandeh@gmail.com
[2] Institute for Astronomy, University of Hawai'i at Manoa, 2680 Woodlawn Drive, Hawai'i, HI 96822, USA
[3] Astrophysics Research Institute, Liverpool John Moores University, IC2, Liverpool Science Park, 146 Brownlow Hill, Liverpool, L3 5RF, UK
[4] Carnegie Observatories, Las Campanas Observatory, Casilla 601, La Serena, Chile
[5] European Southern Observatory, Alonso de Córdova 3107, Casilla 19, Santiago, Chile
[6] Homer L. Dodge Department of Physics and Astronomy, 440 West Brooks Street, Room 100, Norman, OK 73019, USA
[7] Observatories of the Carnegie Institution for Science, 813 Santa Barbara Street, Pasadena, CA 91101, USA
[8] Department of Physics, University of California, 1 Shields Avenue, Davis, CA 95616-5270, USA
[9] Private Astronomer, USA
[10] Facultad de Ciencias Astronómicas y Geofísicas, Universidad Nacional de La Plata, Instituto de Astrofísica de La Plata (IALP), CONICET, Paseo del Bosque S/N, B1900FWA La Plata, Argentina
[11] Institute of Space Sciences (ICE, CSIC), Campus UAB, Carrer de Can Magrans, s/n, E-08193 Barcelona, Spain
[12] DARK, Niels Bohr Institute, University of Copenhagen, Jagtvej 128, DK-2200 Copenhagen, Denmark
[13] Leibniz Supercomputing Centre (LRZ), Boltzmannstr. 1, D-85748 Garching, Germany
[14] Department of Physics and Astronomy, Aarhus University, Ny Munkegade, DK-8000 Aarhus C, Denmark
[15] Division of Physics, Mathematics, and Astronomy, California Institute of Technology, Pasadena, CA 91125, USA
[16] Harvard-Smithsonian Center for Astrophysics, 60 Garden Street, Cambridge, MA 02138, USA
[17] Gordon and Betty Moore Foundation, 1661 Page Mill Road, Palo Alto, CA 94304, USA
[18] George P. and Cynthia Woods Mitchell Institute for Fundamental Physics and Astronomy, Department of Physics and Astronomy, Texas A&M University, College Station, TX 77843, USA
[19] Department of Astronomy, University of Texas, 1 University Station C1400, Austin, TX 78712, USA
[20] Max-Planck Institut fur Astrophysik, Karl-Schwarzschild-Str. 1, D-85741 Garching, Germany
[21] Department of Astronomy and Steward Observatory, University of Arizona, 933 N Cherry Avenue, Tucson, AZ 85719, USA
Received 2021 October 3; revised 2021 November 16; accepted 2021 November 17; published 2022 February 3

Abstract

We present 75 near-infrared (NIR; 0.8−2.5 μm) spectra of 34 stripped-envelope core-collapse supernovae (SESNe) obtained by the Carnegie Supernova Project-II (CSP-II), encompassing optical spectroscopic Types IIb, Ib, Ic, and Ic-BL. The spectra range in phase from pre-maximum to 80 days past maximum. This unique data set constitutes the largest NIR spectroscopic sample of SESNe to date. NIR spectroscopy provides observables with additional information that is not available in the optical. Specifically, the NIR contains the strong lines of He I and allows a more detailed look at whether Type Ic supernovae are completely stripped of their outer He layer. The NIR spectra of SESNe have broad similarities, but closer examination through statistical means reveals a strong dichotomy between NIR "He-rich" and "He-poor" SNe. These NIR subgroups correspond almost perfectly to the optical IIb/Ib and Ic/Ic-BL types, respectively. The largest difference between the two groups is observed in the 2 μm region, near the He I λ2.0581 μm line. The division between the two groups is *not* an arbitrary one along a continuous sequence. Early spectra of He-rich SESNe show much stronger He I λ2.0581 μm absorption compared to the He-poor group, but with a wide range of profile shapes. The same line also provides evidence for trace amounts of He in half of our SNe in the He-poor group.

Unified Astronomy Thesaurus concepts: Galactic and extragalactic astronomy (563); Core-collapse supernovae (304); Type Ib supernovae (1729); Type Ic supernovae (1730); Supernovae (1668)

1. Introduction

Stripped-envelope core-collapse supernovae (SESNe) mark the death of massive stars whose progenitors have been stripped of their outer hydrogen and sometimes even helium envelopes (Clocchiatti et al. 1996). These SESNe are classified into three categories: Types IIb, Ib, Ic (Filippenko et al. 1995; Matheson et al. 2001; Gal-Yam 2017). Type IIb supernovae (SNe IIb) show weak H lines at early times that disappear later and stronger He lines at late times, SNe Ib show no H but prominent He, and SNe Ic show neither H nor He. Broad-line SNe Ic (SNe Ic-BL) constitute a unique subgroup in Type Ic that show broad spectral features and are often associated with long gamma-ray bursts (e.g., Iwamoto et al. 1998; Ashall et al. 2019). These classifications are made mainly using optical spectral features.

It is not yet clear if SESNe arise from single evolved massive stars or interacting binary systems or both. It is also unknown

* This paper includes data gathered with the 6.5 m Magellan Telescopes at Las Campanas Observatory, Chile.

whether these SN subclasses represent distinct explosion mechanisms or progenitor systems. For He-rich SNe Ib and IIb, there have been several detections of progenitor stars, all of which were determined to have $M_{\rm ZAMS} < 25\,M_{\odot}$ (e.g., Cao et al. 2013; Bersten et al. 2014; Fremling et al. 2014; Prentice et al. 2018). For SN Ib iPTF13bvn, a possible binary companion was detected. However, iPTF13bvn is a peculiar Type Ib (Kuncarayakti et al. 2015; Folatelli et al. 2016). Progenitor detections for SNe IIb are more common than SNe Ib, including SN 1993J (Aldering et al. 1994; Cohen et al. 1995), SN 2008ax: (Li 2008), SN 2013df (Van Dyk et al. 2014), and SN 2011dh (Maund et al. 2011; Van Dyk et al. 2011; Bersten et al. 2012; Ergon et al.2015).

To date, there has yet to be a conclusive direct detection of the progenitor of a SN Ic, although Van Dyk et al. (2018) and Rho et al. (2021) found possible evidence for the progenitors of SNe Ic SN 2017ein and SN 2020bvc, respectively. A study by Beasor et al. (2021) suggested that for masses below 27 $M_{\odot}$, the single star pathway is unlikely for the production of Wolf-Rayet stars and SESNe. Commonly, WO and WC Wolf-Rayet stars have been proposed as possible progenitors for SNe Ic (e.g., Crowther 2007; Dessart et al. 2011; Yoon 2015).

It has long been debated as to how SESNe lose their outer envelopes, especially since their progenitor type and configuration are uncertain. Some of the scenarios that could cause copious mass loss include: (i) eruptions (Smith 2006; Smith & Owocki 2006), (ii) radiation-driven winds (Heger et al. 2003b; Smith 2006; Pauldrach et al. 2012), (iii) stripping from a common envelope in a binary system (Nomoto 1984, 1987; Podsiadlowski et al. 1993; Woosley et al. 1995; Wellstein & Langer 1999; Wellstein et al. 2001; Pols & Dewi 2002; Heger et al. 2003b; Podsiadlowski et al. 2004), (iv) fast rotations in Be stars (Massa 1975; Kogure & Hirata 1982; Slettebak 1988; Meynet & Maeder 2005; Meynet et al. 2005; Owocki 2006), or a combination of the above. Each of these scenarios has a different dependence on and relation with the initial mass of the progenitor.

It is not clear if there is a continuum of properties between sub-types of SESNe or if each sub-type points to a separate physical origin. The continuity between Type Ib and Ic hints at possible connections. The residual He I in SNe Ic has been studied for some time but with uncertain results (e.g., Hachinger et al. 2012; Piro & Morozova 2014; Prentice et al. 2018; Dessart et al. 2020; Williamson et al. 2021).

Teffs et al. (2020) concluded that one cannot hide a significant mass of He without line formation at some epoch, and the low He mass in bare C/O core models at 8×10^{51} ergs (8 foe) still produce NIR He I lines but not strong optical He I lines. As the mass of He in the He-poor/He-rich models increases, the He I lines become more apparent. Challenges in identifying residual He are exacerbated by the fact that the Na I D lines are in the same wavelength region (~5875–5890 Å) as the strongest He I line in the optical. In most SNe Ic, a small amount of He may be present but the lack of excitation by gamma-rays could cause some of the He to be effectively hidden (Lucy 1991; Hachinger et al. 2012; Piro & Morozova 2014). With NIR spectroscopy, we can begin to assess the nature of SESNe, for example, the He I lines. The NIR region contains two strong He I lines: λ1.0830 μm and λ2.0581 μm. The current published sample size of NIR spectra is limited, and there have been only a few objects with rapid-cadence coverage (e.g., Taubenberger et al. 2011; Drout et al. 2016). Here, we present and analyze 75 NIR spectra of 34 SESNe, with the aim of providing a better understanding of the origins of SESNe. The spectra were obtained as part of the second phase of The Carnegie Supernova Project (CSP-II; Phillips et al. 2019).

The main focus of this work is to identify the ions responsible for the prominent features near 1 μm and 2 μm, specifically the presence of He. In Section 2, the observations and the sample characteristics are presented. Section 3 describes how the dominant ions for the most prominent spectral features are identified. Section 4 presents our spectroscopic measurements, including velocities and pseudo-equivalent widths for several lines. The principal component analysis (PCA) of the data is presented in Section 5. The limitations of our interpretations of the data and comparisons to models are discussed in Section 6. Finally, a summary of conclusions is given in Section 7.

2. Observations and Sample

We present the largest homogeneous NIR spectroscopic sample of SESNe published to date obtained as part of CSP-II, a four-year NSF-supported project between 2011 and 2015. The project covered four observing campaigns spanning 7–8 months each from October to May centered on the Chilean summer. The NIR spectroscopy program was a vital component of the CSP-II (Hsiao et al. 2019) with the vast majority of the entire CSP-II data obtained using the Folded-port Infrared Echellette (FIRE; Simcoe et al. 2013) mounted at Baade telescope at Las Campanas Observatory (LCO). All 75 NIR spectra of this sample were taken with FIRE. The data can be downloaded from our website.[22] The spectra were observed, reduced, and corrected for telluric absorption following the steps described by Hsiao et al. (2019).

The main aim of the NIR spectroscopy program was to obtain high signal-to-noise ratio (S/N) spectra of nearby SNe in order to construct an SN Ia spectral template for K-correction estimates as well as to study the physical origins of SNe of all types. Therefore, the majority of the CSP-II targets are nearby and at lower redshifts. The mean heliocentric redshift of our SESNe sample is $z = 0.015$ with the distribution shown in Figure 1(a). The redshifts of the host galaxies were mainly obtained from the NASA/IPAC Extragalactic Database (NED).[23] Two exceptions are OGLE-2014-SN-067 and SN 2013fq. The host galaxy redshift of OGLE-2014-SN-067 was determined using narrow host [O III] and [N II] emission lines present in an optical spectrum taken on 2014 August 29 UT (Childress et al. 2014) with the Wide Field Spectrograph (WiFeS) on the Australian National University (ANU) 2.3 m telescope (Childress et al. 2016). The WiFeS spectrum of SN 2013fq taken on 2013 September 19 UT also showed narrow emission lines from the host galaxy indicating a heliocentric redshift of 0.0113 (Parker et al. 2013). Table 1 lists host names and heliocentric redshifts.

The classifications for the SNe in our sample were determined using optical spectra as close to maximum light as possible. Note that these classification determinations were independent of any NIR spectroscopic information. The details of the optical classifications and the full list of the spectra used are presented in Appendix A. Each of the types IIb, Ib, Ic, and Ic-BL is represented in the sample with a handful of SNe (Figure 1(b)).

In this work, the phases of the NIR spectra are labeled relative to the time of B-band maximum unless otherwise noted. For 11 of the objects in the sample, optical photometric follow-up

[22] https://csp.obs.carnegiescience.edu/data
[23] http://ned.ipac.caltech.edu/

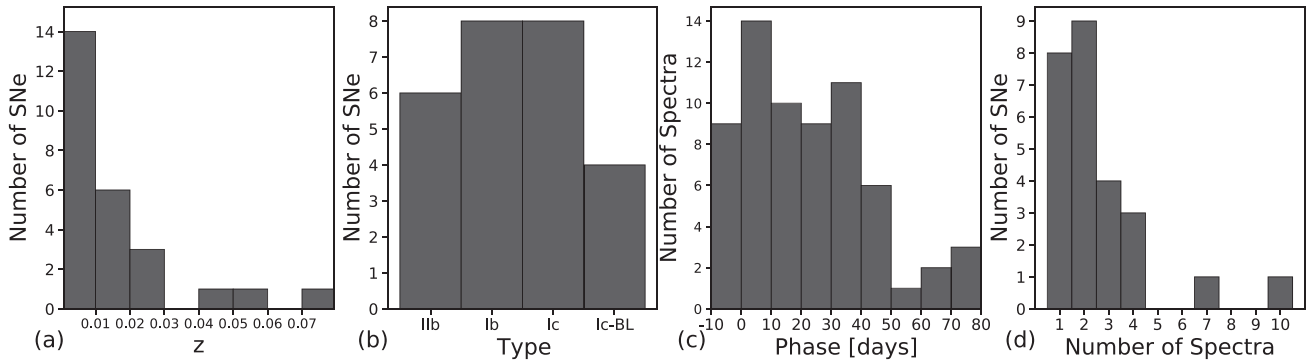

Figure 1. Sample characteristics expressed in four histograms: (a) the distribution of the sample SNe with respect to heliocentric redshift, the SNe with a redshift higher than 0.04 are SN 2013co, LSQ13ddu, and LSQ13lo, (b) the distribution of SNe with respect to Type, (c) the distribution of the NIR spectra with respect to phase, and (d) the number of SESNe with and without time-series observations. The majority of the SNe only have one NIR spectrum. The SNe with the best coverage are SN 2013ge with 10 and SN 2014L with 7 NIR spectra.

Table 1
Host galaxy and SN Phase Information

SN	Host	Redshift[a]	No. of Spec	$MJD_{B_{max}}$ Day	Source of $MJD_{B_{max}}$[b]
ASASSN-14az	WISEA J234448.30-020653.1	0.0067	3	56815.0 ± 2.0	SNID
LSQ13abf	WISEA J114906.60+191006.2	0.0208	1	56417.3 ± 0.5	Stritzinger et al. (2020)
LSQ13cum	WISEA J001507.27-240543.4	0.0260	3	56604.7 ± 0.5	CSP-II
LSQ13ddu	WISEA J035849.18-292508.5	0.0584	2	56626.0 ± 0.2[c]	Clark et al. (2020)
LSQ13doo	UGCA 247	0.0065	2	56599.0 ± 2.0	SNID
LSQ13lo	WISEA J142638.77+033018.1	0.0717	1	56377.9 ± 0.2	CSP-II
LSQ14akx	WISEA J143405.47-073936.5	0.0228	4	56750.5 ± 0.3	CSP-II
iPTF13bvn	NGC 5806	0.0045	3	56473.5 ± 0.5	Fremling et al. (2016)
SN 2011hs	IC 5267	0.0057	2	55884.8 ± 0.1	CSP-II
SN 2012P	NGC 5806	0.0045	2	55948.5 ± 0.5	Fremling et al. (2016)
SN 2012ap	NGC 1729	0.0121	1	55973.5 ± 0.2	CSP-II
SN 2012au	NGC 4790	0.0045	2	55885.0 ± 1.0	Bufano et al. (2014)
SN 2012hf	NGC 3469	0.0155	2	56259.1 ± 1.4	CSP-II
SN 2012hn	NGC 2272	0.0071	1	56032.5 ± 1.0	Valenti et al. (2014)
SN 2013ak	ESO 430- G 020	0.0034	4	56366.1 ± 1.8	Pessi et al. (2019)
SN 2013co	WISEA J125550.49+303042.5	0.0497	1	56425.0 ± 2.0	SNID
SN 2013dk	NGC 4038	0.0055	3	56476.0 ± 2.0[d]	Elias-Rosa et al. (2013)
SN 2013ek	NGC 6984	0.0156	2	56496.9 ± 1.1	CSP-II
SN 2013fq	⋯	0.0113	1	56550.0 ± 2.0	SNID
SN 2013ge	NGC 3287	0.0043	10	56615.7 ± 1.5	Drout et al. (2016)
SN 2014L	M99	0.0080	7	56693.2 ± 0.2	Zhang et al. (2018)
SN 2014ad	MRK 1309	0.0057	4	56735.1 ± 0.2	Sahu et al. (2018)
SN 2014ar	ESO 266- G 015	0.0106	2	56770.8 ± 0.1	CSP-II
SN 2014df	NGC 1448	0.0039	2	56799.0 ± 2.0	SNID
SN 2014eh	NGC 6907	0.0106	1	56973.2 ± 0.2	CSP-II
SN 2015Y	NGC 2735	0.0082	1	57136.3 ± 0.2	CSP-II

Note.
[a] Heliocentric redshift.
[b] Source of the light curves used to determine the time of maximum if available; or using SNID in case of light curve unavailability.
[c] With respect to LSQ-*gr* band maximum.
[d] With respect to *V*-band maximum.

observations, obtained with the 1 m Swope Telescope at LCO, were available to determine the time of maximum. We further relied on previously published light curves for 10 other SNe. The *B*-band light curves (unless otherwise noted) were then interpolated with Gaussian processes using the package included in SuperNovae in object-oriented Python[24] (`SNooPy`; Burns et al. 2011) in order to determine the time of maximum. For five SNe in the sample with no usable photometry, we used their optical spectra and the SuperNova IDentification code `SNID v5.0` (Blondin & Tonry 2007) with Ib/c templates from Liu & Modjaz (2014) to estimate the phase. The SNID-determined phases were assigned an uncertainty of 2.0 days, approximately equal to the largest uncertainty in the time of maximum determined using light curves. Panel (c) of Figure 1 shows the distribution of spectra with respect to phase. The time of maximum and the method for determining it are listed in Table 1 for each SN. Note that this table includes 26 SNe with both optical classification and a time of maximum

[24] https://csp.obs.carnegiescience.edu/data/snpy

estimate. The eight SNe in our sample without either optical classification or a time of maximum are listed in Appendix B and were excluded from our analyses. The journal of observations for the 67 NIR spectra of 26 SNe included in our analyses is shown in Table 2.

This sample includes time-series NIR spectroscopic sequences for nine SNe with three NIR spectra or more (Figure 1(d)). SN 2013ge, a SN Ic, has the best time coverage in the sample with 10 spectra spanning from near maximum light to approximately 80 days past maximum (Figure 2). Time-series spectroscopy for all remaining SESNe with two or more spectra are presented in Figure 3. There are several SNe with only one NIR spectrum each. These spectra were mostly taken for classification purposes and are presented in Figure 4.

Striving for an unbiased sample of SNe Ia, CSP-II prioritized the follow-up of objects discovered by untargeted transient surveys (Phillips et al. 2019). Of the 26 SNe we used in our analyses, 46% were discovered by untargeted surveys, including the All-Sky Automated Survey for SuperNovae (ASAS-SN; Shappee et al. 2014; Holoien et al. 2017), Catalina Real-Time Transit Survey (CRTS; Djorgovski et al. 2011), La Silla-Quest Low Redshift Survey (LSQ; Baltay et al. 2013), and the Palomar Transient Factory (PTF; Law et al. 2009).

3. Line Identification

In this section, we attempt to identify the ions responsible for the main features in the NIR spectra and describe their evolution over time. This can help us investigate the properties of the progenitor stars of SESNe. The line identifications given in Taubenberger et al. (2006), Mazzali et al. (2010), Taubenberger et al. (2011), Bufano et al. (2014), and Ergon et al. (2015) were used as a guide. The most prominent P Cygni line of SESNe is just a redward of 1 μm, regardless of the SN class. To discern whether the ion responsible for this 1 μm feature is He I λ1.0830 μm, we would expect to see other He I lines, therefore the absorption near 2 μm becomes especially important. We will refer to these two as the 1 μm and 2 μm features, respectively, in the remaining text. The line identifications are presented in Figure 5.

3.1. Paγ λ1.0938 μm, Paβ λ1.2818 μm, Paα λ1.8750 μm, and Brγ λ2.1655 μm

The most prominent features observed in SNe II are produced by hydrogen. Paγ λ1.094 μm is located in the 1 μm region that is heavily dominated by the He I λ1.0830 μm line, thus not easily discernible. Paβ is detected in the <29 days spectra of all SNe IIb in the sample, except ASASSN-14az, an SN that seems to be featureless around 1.2 μm. In the case of SN 2013ak, assuming this line is Paβ, the emission feature seems to be blueshifted in the day 5 spectrum (shown in the left panel of Figure 5) but not in the day 17 one (shown in the right panel of Figure 5). Also, note that a P Cygni profile is detected at the same wavelength ($\sim$1.26 μm) in the majority of the SNe Ib and Ic in the sample as well. In SNe IIb, this feature is concurrent with Paα, Hα, Hβ, and Hγ. Thus, we identify it as Paβ. Conversely, in SNe Ib and Ic, this feature appears with C I lines in both the optical and NIR. Additionally, we do not detect any other H lines in these SNe. Therefore, we identify this feature as C I λ1.2614 μm. Paα λ1.8750 μm lies in a region with heavy telluric absorption, even when there is an adequate signal from the SN after telluric correction, Paα λ1.8750 μm is not easily detectable. However, we detect Paα in SN 2013ak and LSQ14akx. The Brγ λ2.1655 μm line is located near where we see the emission feature of the He I λ2.0581 μm line, therefore it may be heavily dominated by He I. Due to the presence of He I in SNe IIb and Ib, it is difficult to distinguish between a SN IIb and a SN Ib using NIR spectroscopy alone. In Figure 5, we have shown a Type II SN with H I lines marked in blue for comparison with SESNe.

3.2. He I λ1.0830 μm, λ1.7002 μm, and λ2.0581 μm

He I λ1.0830 μm forms a distinct and prominent P Cygni in the spectra of SNe IIb and Ib, and possibly contributes to the 1 μm feature in SNe Ic. This profile is produced by the 2^3S–2^3P transition. He I λ1.0830 μm line is about 5–15 times stronger than the He I λ2.0581 μm line and much stronger than any optical He I lines. The He I λ2.0581 μm feature can also be easily detected in the spectra of SNe IIb and Ib. This line is formed by 2^1S–2^1P transition. The other He I at λ1.7002 μm is much weaker than the other mentioned He I lines, but it can be found in some of the SNe in the sample. He I lines are identified in orange in Figure 5. One of the main goals of this work is to determine whether He is present in SNe Ic. This topic is explored in detail in Section 6.

3.3. C I λ0.9093 μm, λ0.9406 μm, λ0.9658 μm, λ1.0693 μm, λ1.2614 μm, and λ2.1259 μm

One or more of the three C I lines: λ0.9093 μm, λ0.9406 μm, λ0.9658 μm are detected in most spectra of this sample regardless of the type, even though they are much weaker than the C I λ1.0693 μm line. They may be blended with O I λ0.9264 μm or Mg II λ0.9227 μm, making it challenging to distinguish their contribution to the weak lines in this region. On the other hand, the C I λ1.0693 μm line is one of the strongest lines in the NIR. It also coincides with the strong 1 μm feature present in all SESNe in the sample. We therefore consider C I λ1.0693 μm one of the possible main contributors to the 1 μm feature. A detailed examination of this profile and contributions from He I λ1.0830 μm and C I λ1.0693 μm are presented in Section 6. We detect a feature in the majority of the SNe in this sample around 1.26 μm, that could be formed by C I λ1.2614 μm. Other C I lines may also form weaker features, such as λ1.1330 μm, λ1.1754 μm, and λ1.4543 μm. The C I λ2.1259 μm line may contribute to the absorption feature near 2 μm, also discussed in Section 6. In Figure 5, C I lines are marked in purple.

3.4. O I λ0.9264 μm and λ1.1290 μm

The O I λ1.1290 μm line is the strongest O I line in the NIR. It can be identified in most spectra as a weak absorption, situated just redward of the prominent 1 μm feature. Over time, this feature becomes more apparent. The λ0.9264 μm feature is another O I line that is present in many of the SNe in the sample. The O I lines are marked in brown in Figure 5.

3.5. Mg I λ1.1828 μm, λ1.4878 μm, and λ1.5033 μm

Mg I λ1.4878 μm and λ1.5033 μm form a narrow emission-like feature that is characteristic of most evolved NIR spectra of SESNe. They sometimes form a single emission and sometimes

Table 2
Journal of Observations

SN	UT date	MJD Day	Phase Day	Telluric STD	Airmass	Total Exp Time s
ASASSN-14az	2014-06-06	56814.9	−1.0	HD4329	1.4	507.2
ASASSN-14az	2014-06-17	56824.9	+10.4	HIP116886	1.1	507.2
ASASSN-14az	2014-07-10	56847.9	+33.4	HD8325	1.1	1014.4
LSQ13abf	2013-05-19	56430.6	+14.2	HIP59861	1.6	1268.0
LSQ13cum	2013-11-14	56609.7	+5.5	HD4329	1.5	1268.0
LSQ13cum	2013-11-20	56615.7	+11.4	HD8325	1.4	1268.0
LSQ13cum	2013-11-30	56625.6	+20.0	HD2339	1.2	1014.4
LSQ13ddu	2013-12-09	56635.2	+9.0	HD27803	1.4	1902.0
LSQ13ddu	2013-12-14	56640.2	+14.0	HD33243	1.3	1521.6
LSQ13doo	2013-11-30	56625.8	+27.3	HD106010	1.5	507.2
LSQ13doo	2013-12-20	56645.8	+47.3	HD96781	1.4	317.0
LSQ13lo	2013-03-25	56375.8	−2.6	HD117248	1.2	1394.8
LSQ14akx	2014-03-18	56733.8	−16.2	HD157334	1.1	1014.4
LSQ14akx	2014-03-25	56740.8	−9.1	HD129684	1.1	2028.8
LSQ14akx	2014-04-23	56769.7	+20.0	HD125062	1.1	1521.6
LSQ14akx	2014-06-06	56813.6	+63.6	HD125062	1.2	760.8
iPTF13bvn	2013-07-16	56488.6	+30.2	HD134240	1.6	951.0
iPTF13bvn	2013-07-29	56501.5	+43.1	HD100852	1.3	1268.0
iPTF13bvn	2013-09-02	56536.5	+78.1	HD125062	1.8	760.8
SN 2011hs	2011-12-18	55912.6	+28.5	HD221793	1.4	465.2
SN 2011hs	2011-12-21	55916.0	+31.0	HD223296	1.7	507.2
SN 2012P	2012-01-19	55944.9	−3.6	HD23722	1.7	380.4
SN 2012P	2012-03-03	55988.8	+40.3	HD147295	1.2	1268.0
SN 2012ap	2012-03-03	55988.5	+14.8	HD290322	1.3	1268.0
SN 2012au	2012-04-18	56034.7	+28.2	HD109587	1.2	960.0
SN 2012au	2012-04-21	56037.7	+31.2	HD109587	1.3	960.0
SN 2012hf	2012-12-03	56263.8	+5.2	HD90738	1.2	2219.0
SN 2012hf	2012-12-20	56280.7	+22.2	HD105992	1.2	3170.0
SN 2012hn	2012-04-19	56036.0	+3.0	HD50963	1.2	1200.0
SN 2013ak	2013-03-20	56370.6	+4.9	HD67526	1.0	380.4
SN 2013ak	2013-03-25	56375.5	+10.0	HD77562	1.0	380.4
SN 2013ak	2013-04-01	56382.6	+17.0	HD67638	1.5	253.6
SN 2013ak	2013-05-18	56430.4	+64.8	HD66018	1.1	507.2
SN 2013co	2013-05-19	56430.6	+6.1	HIP59861	2.0	1268.0
SN 2013dk	2013-06-25	56467.5	−8.5	HD94359	1.1	360.0
SN 2013dk	2013-07-15	56488.4	+12.5	HD97919	1.1	1014.4
SN 2013dk	2013-07-29	56501.5	+25.5	HD100852	1.5	1268.0
SN 2013ek	2013-07-29	56501.7	+4.8	HD200523	1.1	1902.0
SN 2013ek	2013-09-02	56536.7	+38.0	HD203999	1.2	507.2
SN 2013fq	2013-09-18	56553.0	+1.0	HD196106	1.1	507.2
SN 2013ge	2013-11-20	56615.9	−1.9	HD284582	2.1	507.2
SN 2013ge	2013-11-30	56625.9	+7.8	HD106010	1.9	380.4
SN 2013ge	2013-12-09	56634.8	+16.7	HD96781	1.9	380.4
SN 2013ge	2013-12-14	56639.8	+21.7	HD96781	1.8	507.2
SN 2013ge	2013-12-20	56645.8	+27.7	HD96781	1.8	507.2
SN 2013ge	2013-12-27	56652.8	+34.7	HD96781	1.9	507.2
SN 2013ge	2014-01-01	56657.8	+39.6	HD96781	1.6	507.2
SN 2013ge	2014-01-09	56665.9	+47.7	HD96781	1.6	380.4
SN 2013ge	2014-01-14	56670.8	+52.6	HD96781	1.6	507.2
SN 2013ge	2014-02-08	56695.8	+77.8	HD96781	1.7	380.4
SN 2014L	2014-02-08	56695.9	+1.6	HD96781	1.5	380.4
SN 2014L	2014-02-15	56702.8	+8.6	HD96781	1.4	570.6
SN 2014L	2014-02-22	56709.8	+15.5	HD96781	1.4	380.4
SN 2014L	2014-02-27	56714.8	+20.5	HIP59861	1.4	507.2
SN 2014L	2014-03-10	56725.7	+31.4	HD96781	1.5	507.2
SN 2014L	2014-03-18	56733.7	+39.4	HD96781	1.4	507.2
SN 2014L	2014-03-25	56740.7	+46.4	HD96781	1.4	507.2
SN 2014ad	2014-03-18	56733.6	−1.0	HD105992	1.3	507.2
SN 2014ad	2014-03-25	56740.7	+6.2	HD97919	1.2	507.2
SN 2014ad	2014-04-23	56769.7	+35.0	HD97919	1.1	1014.4
SN 2014ad	2014-06-06	56813.6	+79.0	HD122435	1.6	760.8
SN 2014ar	2014-04-23	56769.7	−0.6	HD105011	1.2	1521.6
SN 2014ar	2014-06-06	56813.6	+43.3	HD122435	1.6	760.8
SN 2014df	2014-06-06	56814.4	+2.0	HD18620	2.5	507.2
SN 2014df	2014-07-10	56848.4	+36.0	HD23722	1.3	1014.4
SN 2014eh	2014-11-05	56965.5	−7.2	HD202633	1.1	1014.4
SN 2015Y	2015-04-12	57123.5	−12.2	HD96781	1.7	1521.6

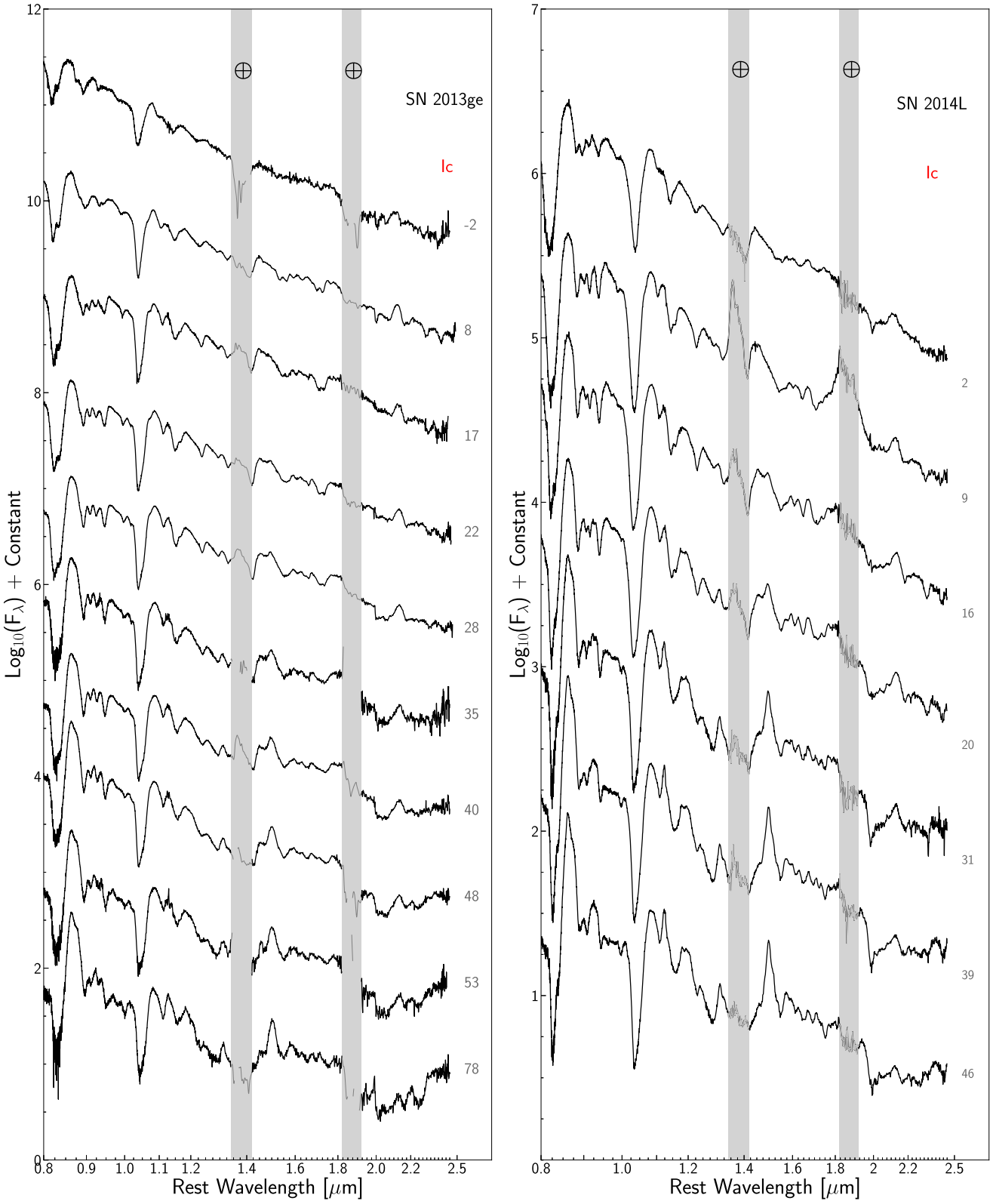

Figure 2. Time-series NIR spectra of the Type Ic SNe, SN 2013ge, and SN 2014L. These two SNe have the best time coverage of the sample. The two gray bands mark regions that have high telluric absorptions from the atmosphere. The number on the right side of each spectrum is the phase relative to the *B*-band maximum.

form a "double-horned" emission with peaks that coincide with the rest wavelengths of the two lines. The absorption component of the P Cygni profile may be blended with the emission component of C I λ1.454 μm, be affected by the telluric region, or it could be a result of de-excitation from higher levels. The feature emerges around 30 days past maximum for nearly all SNe in the sample and becomes stronger over time. The weaker Mg I λ1.1828 μm line lies in the telluric region, and it is

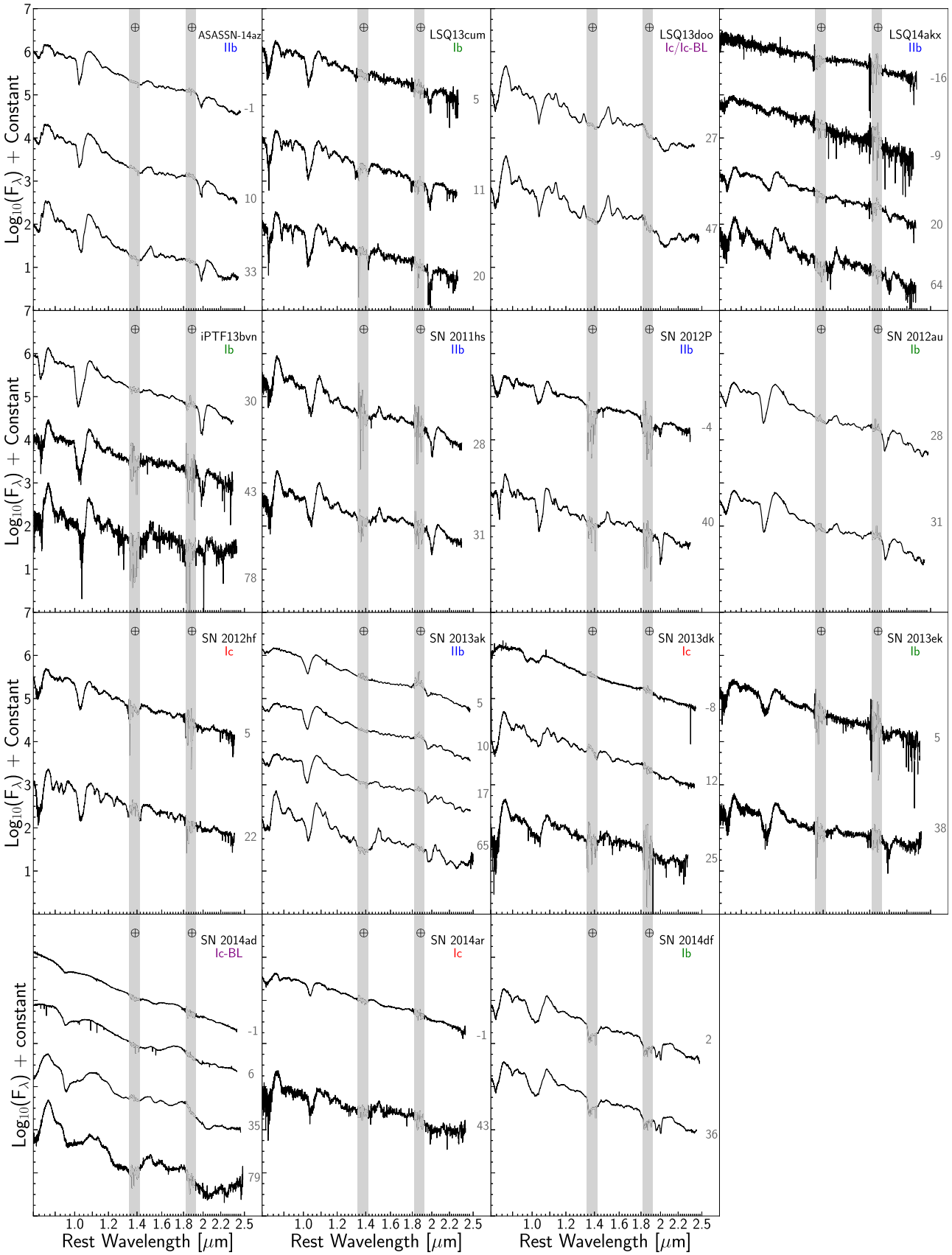

Figure 3. Time-series NIR spectra of the SNe with two or more spectra. Note that the time series of SN 2013ge and SN 2014L are shown separately in Figure 2. The phase relative to the maximum light of each spectrum and the type of each SN are also labeled. The wavelength regions with strong telluric absorptions are marked with vertical gray bands.

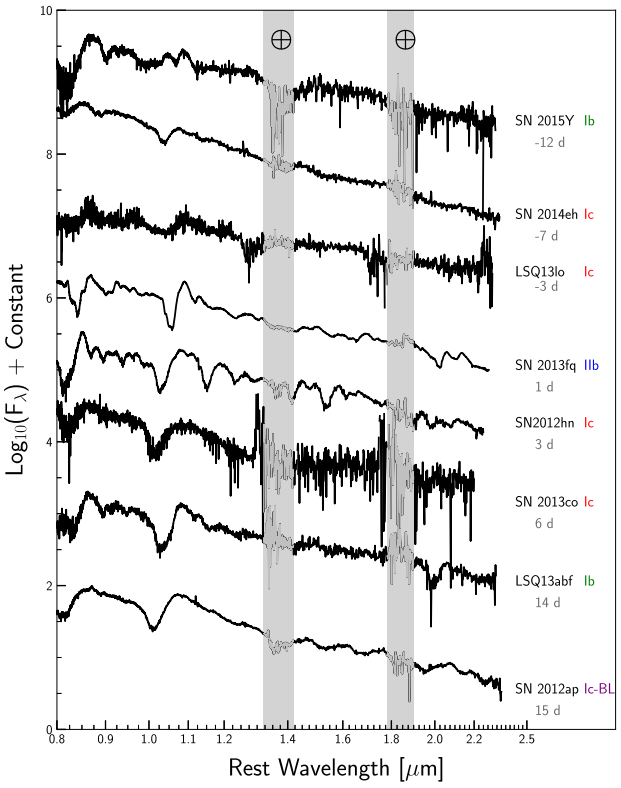

Figure 4. Spectra of the SNe with a single spectrum within the sample that have optical spectra and/or photometry available for phase estimation and spectroscopic classification. The feature blueward of the telluric region for SN 2013co is likely an artifact of the observation and not real.

therefore not easily detectable. The Mg I lines are marked in magenta in Figure 5.

3.6. Mg II λ0.9227 μm, λ1.0092 μm, λ1.0927 μm, and λ2.1369 μm

Mg II λ1.0927 μm may be another major contributor to the 1 μm feature. Its effect is examined in detail in Sections 5 and 6. The weaker Mg II λ0.9227 μm and λ1.0092 μm may be blended with C I and O I lines as mentioned in previous subsections. Mg II λ2.1369 μm may also be a contributor to the 2 μm feature. Its separation from He I λ2.0581 μm demonstrates a potential advantage of this region for identifying the ions that are present.

3.7. S I λ0.9223 μm and λ1.0457 μm

S I λ0.9223 μm coincides with Mg II λ0.9227 μm and cannot be separated. S I λ1.0457 μm may also contribute to the prominent 1 μm feature. This line is at the bluest wavelength of all the candidates considered for the 1 μm feature.

3.8. Ca II λλλ 0.8538, 0.8662, 0.8921 μm, λ1.1839 μm, and λ1.1950 μm

The Ca II infrared triplet is present in all of the NIR spectra in this sample. This feature is weak before and around maximum light and becomes progressively stronger over time. The Ca II λ1.1839 μm and λ1.1950 μm lines may also be present but they are not as prominent as the infrared triplet. The Ca II lines are shown in green in Figure 5.

4. Spectroscopic Measurements

To quantify the attributes of the strongest spectral features observed, we measured the pseudo-equivalent widths (pEW) and the velocities at their absorption minima. In particular, we focus on the prominent absorption feature near 1 μm and the weaker absorption feature near 2 μm to discern whether these can be attributed to He I lines. In this section, the details of these measurements are described.

4.1. Equivalent Width

The pEW is used to quantify the strength of a spectral absorption feature. We adopted the formalism for pEW outlined by Folatelli (2004) and Garavini et al. (2007). As the feature boundaries are sometimes ambiguous, the boundary ranges were set manually for each spectrum. We defined the continuum as the straight line connecting the boundaries on the blue and red sides of the absorption feature and used it to normalize the spectrum before the area is integrated. To estimate the uncertainty in the pEW measurement, 100 realizations of simulated spectra were created by varying the flux at each pixel randomly and independently based on its flux error. Furthermore, the blue and red boundaries that define the continuum were also varied randomly for each realization within an average range of 0.006 μm around the chosen boundaries. The median absolute deviation of the 100 pEW measurements multiplied by 1.48 (Rousseeuw & Croux 1993; Leys et al. 2013) was then taken as the 1σ error.

All the spectra in our sample show strong absorption features near 1 μm regardless of the optical spectral type, and most show a weaker absorption near the 2 μm region. Without identifying the ions responsible for these features, we simply present the time evolution of the pEWs in Figure 6. There are large ranges of pEWs for both the 1 μm and the 2 μm features, spanning from a few tens to 500 Å. In SNe IIb, both features have monotonically increasing pEWs as the spectra evolve with time. On average, SNe IIb and Ib show slightly stronger 1 μm features than SNe Ic and Ic-BL. However, if we disregard SNe Ic-BL, the difference between the two groups becomes much more apparent. Also note that the pEW measurements of the 1 μm feature for SN 2014L, a well-sampled SN Ic, are situated in the average of pEWs of the SN IIb/Ib group.

There exists a much stronger dichotomy between the SN IIb/Ib and SN Ic/Ic-BL groups in the strength of the 2 μm feature compared to the 1 μm region. While the pEWs of SNe IIb/Ib span a wide range of ∼150–500 Å, those of SNe Ic/Ic-BL are largely confined to low values of $\lesssim$150 Å with LSQ13doo and SN2013co being the exceptions. The 2 μm feature clearly divides the sample into two distinct groups: NIR "He-rich" and "He-poor" groups with the pEW staying above and below 150 Å over time, respectively. The NIR He-rich and He-poor groups correspond almost perfectly with the optical SN IIb/Ib and SN Ic/Ic-BL groups, respectively.

4.2. Velocity

In order to measure the blueshift velocity of a spectral feature, the wavelength of the absorption minimum is determined by fitting Gaussian functions to the profile via nonlinear least-square minimization (Newville et al. 2014). Again, we focus on the absorption features near 1 μm and 2 μm. In most of our spectra, these features cannot be adequately described by a single Gaussian function as indicated

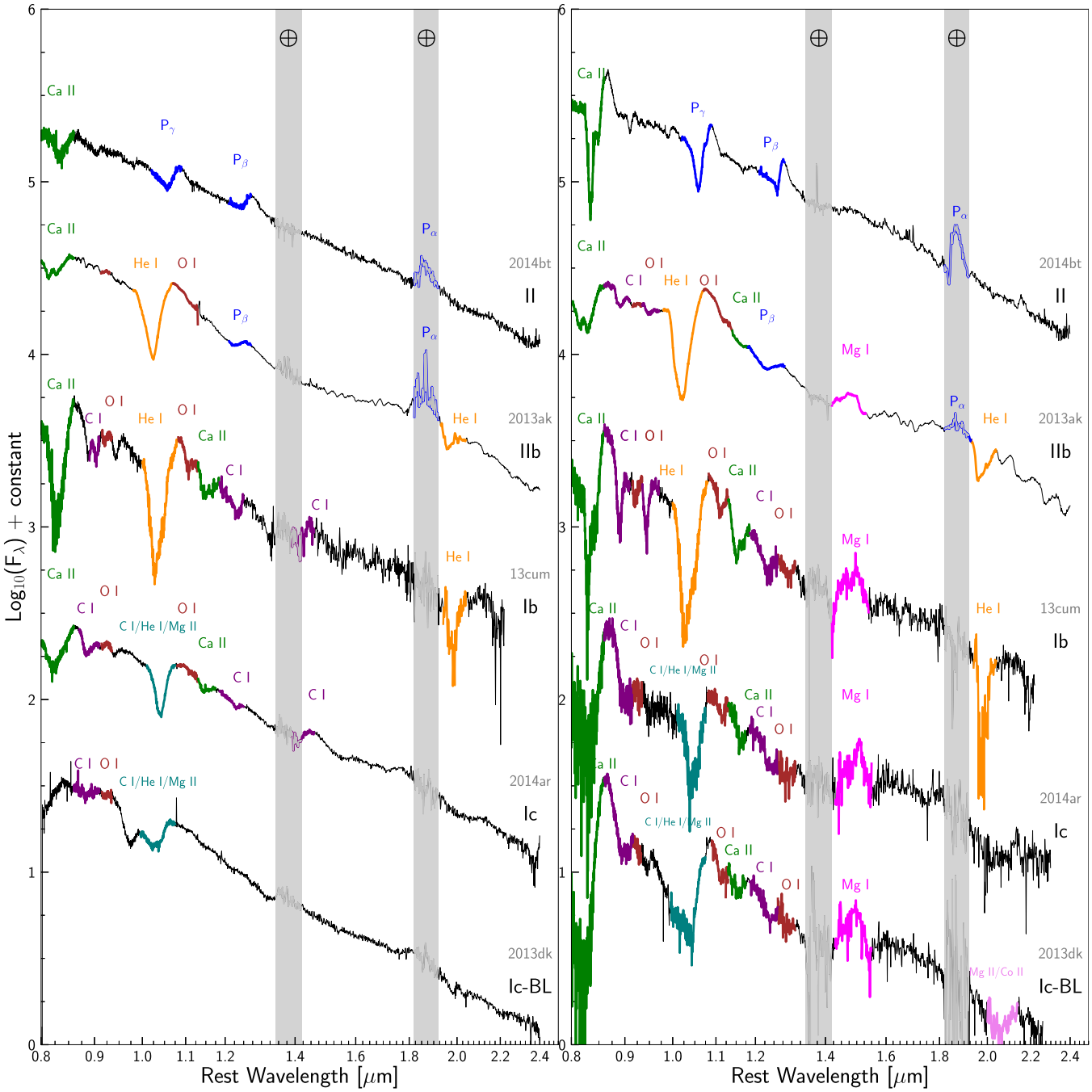

Figure 5. An atlas of NIR spectra of SESNe with absorption feature of prominent lines labeled for comparison. The SNe names and types are labeled on the right-hand side of each spectrum. The left and right panels show spectra around maximum light and around 30 days past maximum, respectively. The gray bands mark the regions with high telluric absorption. The Type II SN 2014bt shown at the top of the figure is for comparison.

by the reduced χ^2 which were $\gg 1$ in these fits. We found that a two-Gaussian function provides the best results for most of our spectra, although there exist a variety of profile shapes. This may indicate the presence of multiple ions or lines formed in large optical depth for the strong 1 μm feature. Detailed discussions are presented in Section 6.

We adopted the same profile boundaries and definition of pseudo-continuum as those used for measuring the pEW. The fit parameters are the wavelength center, width, and depth for each Gaussian component. The wavelength center of the component with the deepest absorption was then taken for the velocity estimate. Each two-Gaussian fit to the 1 μm and 2 μm features is presented in Appendix D. If a fit region has a median S/N ratio of S/N < 5, the spectrum is excluded from the fit. This applies to four spectra in our sample with low signals in the K band. The uncertainty in the wavelength of the absorption minimum and thus the velocity is determined in a similar fashion as that for pEW. Realizations were created to account for the effects of flux errors and uncertain boundary selections. The wavelength of the absorption minimum is determined for each of the 100 realizations. The median absolute deviation of the absorption minimum multiplied by 1.48 was then taken as the 1σ uncertainty.

The wavelengths of the absorption minima for each of the 1 μm and the 2 μm features are shown in Figure 7. There does

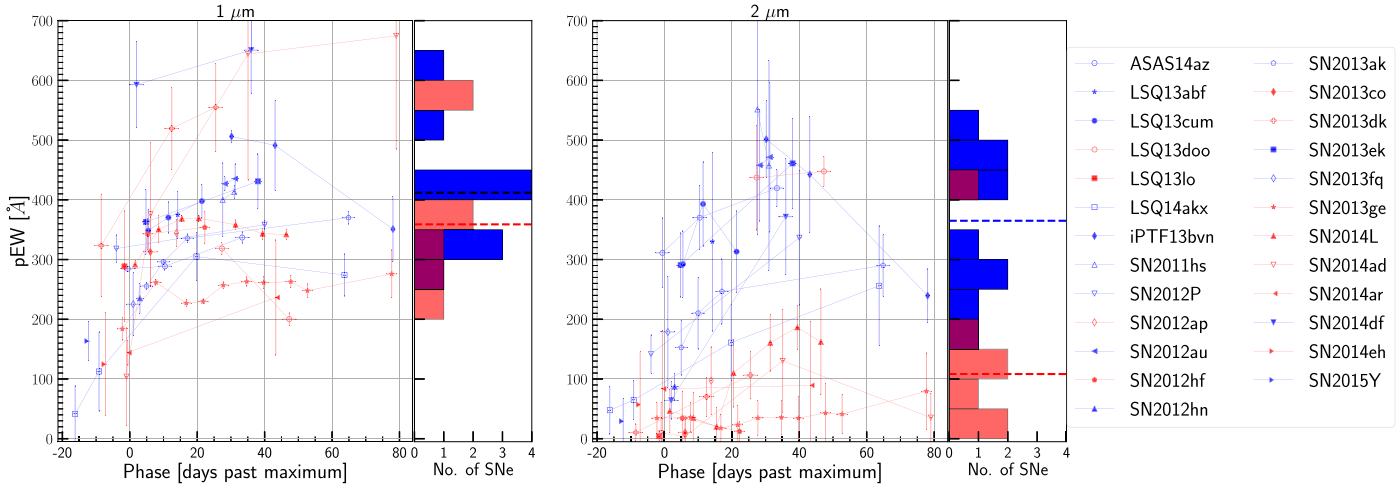

Figure 6. The pEW measurements of the absorption features near 1 μm (left panel) and 2 μm (right panel). The SN IIb/Ib and SN Ic/Ic-BL groups are shown in blue and red, respectively, with filled symbols representing Type Ib/Ic and open symbols representing Type IIb/Ic-BL. To compare the pEW distributions of the SN IIb/Ib vs. SN Ic/Ic-BL groups, histograms are shown for SNe with available pEW measurements interpolated to 30 days past maximum. The blue and red dashed lines on the histograms mark the median pEW for SNe IIb/Ib and SNe Ic/Ic-BL at day 30, respectively.

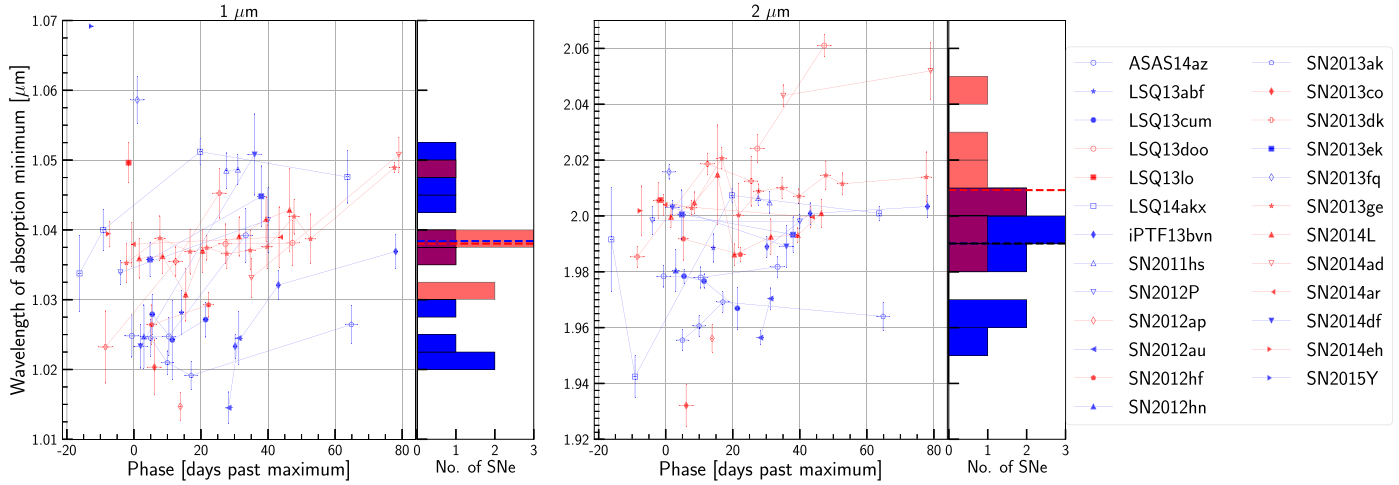

Figure 7. The rest-frame wavelengths of the absorption minima for the 1 μm (left panel) and 2 μm (right panel) features. The histograms are shown for SNe with available wavelength measurements interpolated to 30 days past maximum. The blue and red dashed lines on the histograms mark the median minimum for SNe IIb/Ib and SNe Ic/Ic-BL at day 30, respectively. The symbols and colors are coded as in Figure 6.

not appear to be a significant difference in the location of the 1 μm absorption minimum between the SN IIb/Ib and SN Ic/Ic-BL groups. For the 2 μm feature, there is a slight difference between the two groups. On average, the 2 μm absorption minima of SNe Ic/Ic-BL appear at slightly redder wavelengths than those of SNe IIb/Ib. We convert these wavelengths to velocities for several possible ions and discuss the implications in Section 6.

5. Principal Component Analysis

PCA is a statistical technique that reduces the dimensionality of a data set and thus allows for many applications. The method has been shown to be especially useful for spectroscopic data sets where there are relatively few instances of missing information (e.g., Hsiao et al. 2007; Davis et al. 2019; Williamson et al. 2019). Here, we employed PCA to search for trends in the spectral variations that may otherwise be difficult to detect.

The input data are organized into a fixed rest-wavelength grid, and each spectrum is smoothed and then normalized to have the same *J*-band flux. All spectra were included. The resulting principal components (PCs) are therefore heavily weighted toward a few SNe with many time-series spectra. Standard procedures are followed for the PCA with the mean flux removed, covariance matrix calculated, and diagonalized. The PCs are then ordered according to their eigenvalues, or how much variation in the data they account for.

The first four PCs account for over 90% of the spectral variation. The strength of the first component alone relative to the others tells us how similar the spectra are, confirming that SESNe have broadly similar spectral features in the NIR. The first and second PCs, accounting for ∼76% and ∼10% of the variation, respectively, describe the general time evolution in the spectral features (Figure 8). As the NIR spectra evolve, the strengths of the features increase and the velocities decrease, in general (Section 4).

The third PC only accounts for only ∼4% of the overall spectral variation but describes the differences between the NIR He-rich and He-poor groups (Section 4.1). In Figure 9, the projection of each spectrum onto the third PC versus phase is shown. This PC is largely able to divide the two groups at early

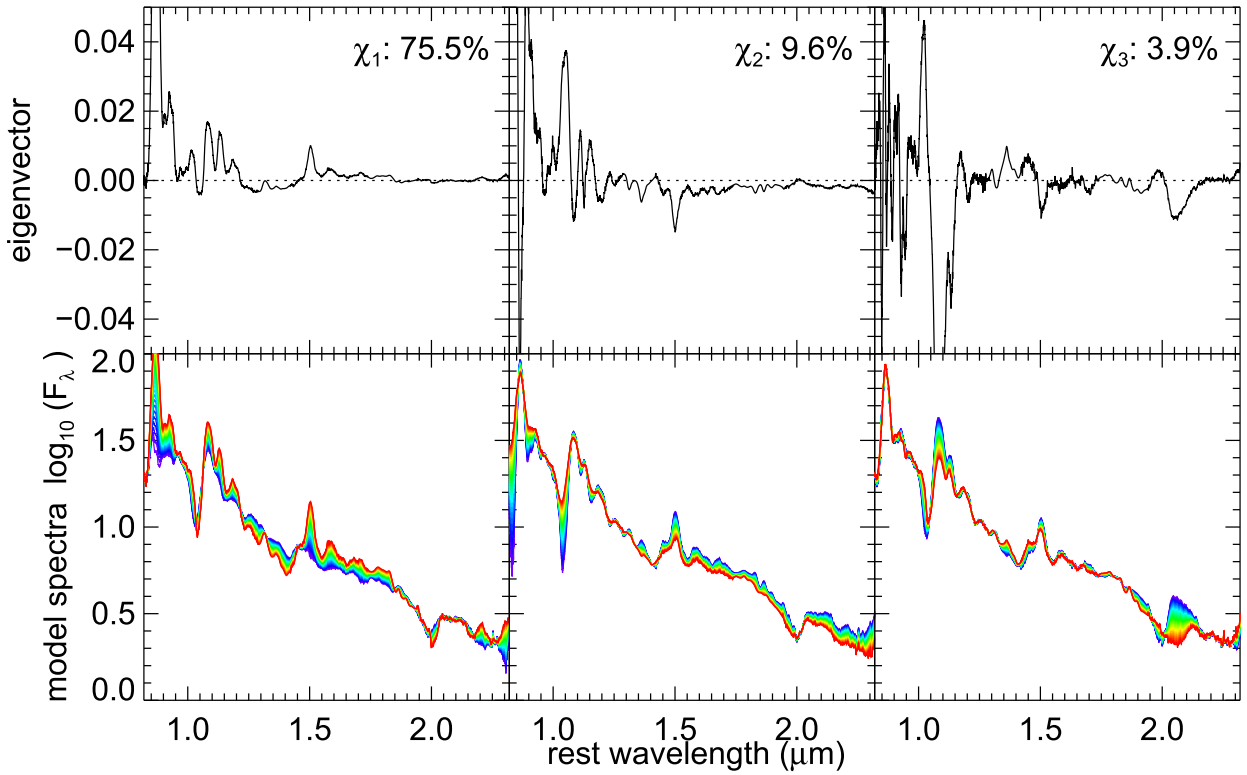

Figure 8. The first, second, and third PCs. The top panels show the eigenspectra, and the bottom panels present the PC-reconstructed spectra. The colored PC-reconstructed spectra represent the 1σ data variation each PC describes. The first three PCs account for 75.5%, 9.6%, and 3.9% of the spectral variations, respectively. The first and second PCs describe the general time evolution in the spectral features, whereas the third PC captures the differences between the SN IIb/Ib and SN Ic/Ic-BL groups, mostly in the 2 μm region.

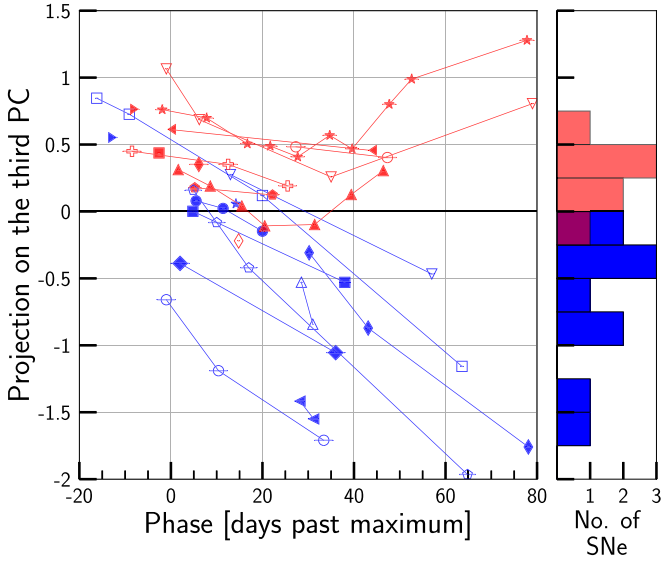

Figure 9. Projection of the spectra on the third PC shown over time. The measurements of the same SN are connected by straight lines. The He-rich Type IIb/Ib and the He-poor Ic/Ic-BL are presented in blue and red, respectively. The third PC is able to separate the He-rich and He-poor groups, especially past roughly one month past maximum. The same symbols from Figure 6 are also used here. The histograms are shown for SNe with available measurements interpolated to 30 days past maximum.

phases with only a few exceptions. The groups then begin to completely diverge starting at roughly one month past maximum. The divergence of the NIR spectral properties again demonstrates that the NIR He-rich and He-poor groups correspond almost perfectly with the optical SN IIb/Ib and SN Ic/Ic-BL groups. It bears repeating here that the classifications are entirely based on optical spectra near maximum light.

Taking a closer look at the differences in the NIR spectroscopic properties between the He-rich and He-poor groups, Figure 10 plots the spectral variations reconstructed by the third PC. Note that the PCs have been smoothed in the regions of heavy telluric absorptions, and those regions are marked in Figure 10. The most discernible differences are observed near the 2 μm region where the He I λ2.0581 μm line resides, confirming the results from Section 4.1. For the He-poor group, while the He I λ2.0581 μm line may be weak, the Mg II λ2.1369 μm may be present further to the red. This suggests that the 1 μm feature may be partially attributable to Mg II λ1.0927 μm for the He-poor group.

Since the strong feature near 1 μm may be attributed to several strong lines such as C I, He I, and Mg II (Section 3), the 2 μm region may indeed be the best region to determine whether He I is present in a NIR spectrum. More subtly, the third PC shows more prevalent He I and Mg I features in He-rich SNe and more prevalent C I and Mg II features in He-poor SNe. These ions are identified using the emission peaks of P Cygni profiles of multiple lines in the PC-reconstructed spectra in Figure 10. In individual spectra, the identifications may be less obvious or individual features may disappear with spectral evolution.

Using the resulting PCs and their correlations, we construct the NIR spectral templates for SESNe that may be useful for a variety of applications. First, the time evolution of the projections on each of the four PCs is specified for each SN type. This is an imperfect process, as there exist variations within each spectral type (see Figure 9). SNe IIb and Ib have indistinguishable projections for the first four PCs, so one spectral template is built for both. This

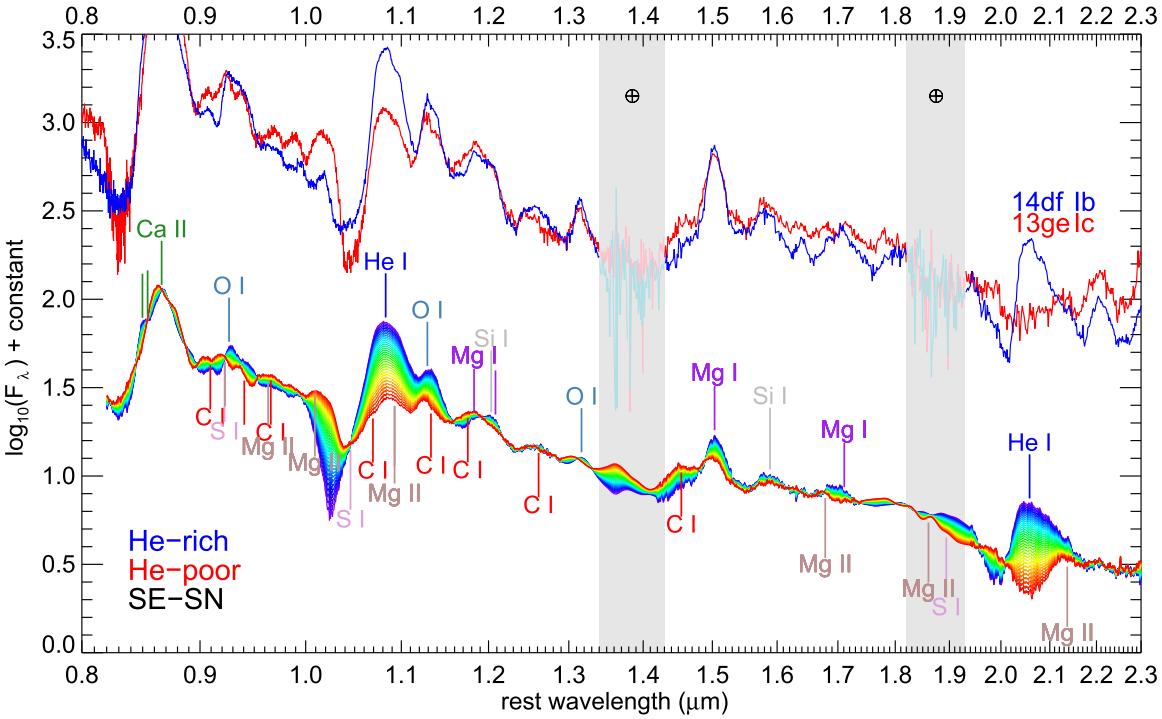

Figure 10. Line identifications of the NIR He-rich and He-poor groups using the third PC. The PC-reconstructed spectra are presented on the bottom representing the spread in the projections shown in Figure 9 (the color range from blue to red represents projections from −2.0 to 1.3). The vertical lines mark the laboratory rest wavelengths of the labeled ions. The 2 μm region shows the largest difference in profile shapes between the two groups. The spectra of SNe 2014df (Ib) and 2013ge (Ic) at late phases are also shown as examples of the He-rich and He-poor groups, respectively.

further supports our assessment that the H Paschen and Brackett series in the NIR are weak for SNe IIb compared to SNe II.

6. Discussion

The main focus of this work is to identify the ions responsible for the prominent features near 1 μm and 2 μm. Specifically, whether they correspond to the He I λ1.0830 μm and λ2.0581 μm lines is of great interest especially for SNe Ic. There are several strong lines that may contribute to the 1 μm feature (Section 3), complicating the analysis. Thus, we use several methods in this section in an attempt to piece together a coherent picture and identify the most likely dominant species for each SN group.

6.1. Line Identifications Through Observables

The 1 μm feature. The strongest He I line at both the optical and the NIR wavelengths is the He I λ1.0830 μm line. Nearly all of the spectra in our sample have a strong absorption near 1 μm making it the natural place to begin our investigation. The profile shape of this feature varies widely, and a two-Gaussian function provides adequate fits in most instances (Section 4.2). This does not automatically assume that there are two lines contributing to the feature, as lines formed in large optical depth can produce a similar shape. Nonetheless, we explore the possibility that the profile is formed by multiple ions.

In Figure 11, the blue and red components of the two-Gaussian functions from the 1 μm profile fits are examined separately, and the velocities are shown assuming several possible ions. Three strong lines in this region were considered: C I λ1.0693 μm, He I λ1.0830 μm, and Mg II λ1.0927 μm. The velocity of the blue component is shown assuming that the main contributor is C I or He I; the velocity of the red component is shown assuming that the main contributor is He I or Mg II. All possibilities explored result in reasonable ranges of velocities, except for a few outliers. Furthermore, on average, we observe that the velocities are decreasing over time. This agrees with the study done by Liu et al. (2016) on the optical spectra of SESNe. It is also worth noting that Liu et al. (2016) showed the biggest difference between SNe IIb/Ib and SNe Ic can be found in the strength of the optical O I line. They also found that SNe Ic show higher velocities for both O I and Fe II optical lines.

As shown in Figure 11, assuming He I for the blue component, velocities of the 1 μm feature range from 12,500 to 20,000 km s^{-1}. For the blue component, He-poor SNe show slightly slower velocities on average than He-rich SNe. As SNe Ic are known to be more energetic explosions (Mazzali et al. 2017), it is not likely that the 1 μm feature is formed by the same ions for both He-poor and He-rich SNe. On the other hand, assuming He I for the red component results in a velocity range of 7000–15,000 km s^{-1}, and a distinction is not seen between the two groups. Assuming C I for the blue component and assuming Mg II for the red component, the resulting velocity ranges are 8000–16,000 km s^{-1} and 10,000–17,500 km s^{-1}, respectively.

The combination of a blue He I and a red Mg II component would mean the Mg layer is situated only slightly below the He layer with significant overlap. Noting that this is true in a spherically symmetric explosion with concentric layers (e.g., Bersten et al. 2012). The combination of a blue C I and a red He I component would mean the C layer is situated slightly above the He layer again with significant overlap. This scenario would require contrived mixing and is not likely to be true. The combination of a photospheric and high-velocity He component or a single He line formed in large optical depth are also possibilities. There are no distinct differences between the He-rich and He-poor groups in the 1 μm region.

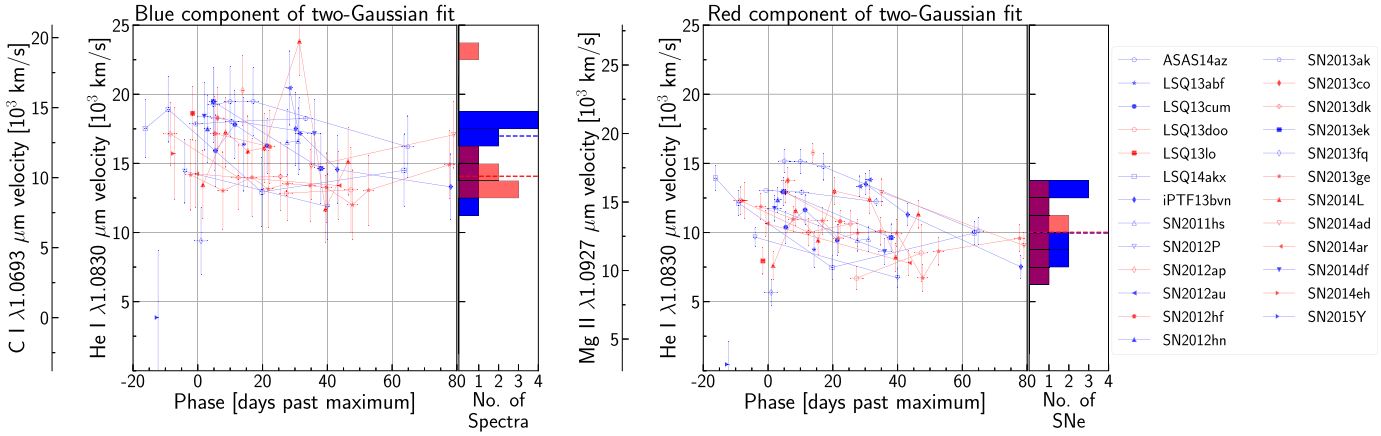

Figure 11. The velocity of the absorption feature at 1 μm, assuming that the two-Gaussian fitting function represents two separate ions. The SN IIb/Ib and SN Ic/Ic-BL groups are shown in blue and red, respectively, with filled symbols representing Type Ib/Ic and open symbols representing Type IIb/Ic-BL. The left panel shows the blue component of the two-Gaussian function. The right panel shows the red component. The assumed ion is indicated for each panel on the *y*-axis. The histograms are shown for SNe with available velocity measurements interpolated to 30 days past maximum. The blue and red dashed lines on the histograms mark the median velocity for SNe IIb/Ib and SNe Ic/Ic-BL at day 30, respectively.

In the case that the entire 1 μm profile is formed by a single line, we then plot the velocities measured from the profile minima of the entire two-Gaussian fit. Again, three possibilities are considered: C I λ1.0693 μm, He I λ1.0830 μm, and Mg II λ1.0927 μm (Figure 12). The resulting velocities also occupy reasonable ranges of 10,000–20,000 km s^{-1} for He I, 5000–15,000 km s^{-1} for C I, and 12,000–22,000 km s^{-1} for Mg II. The velocities would be slightly high for Mg II, with some SNe reaching above 20,000 km s^{-1}, making it unlikely that this feature is formed solely by Mg II. There are also no distinct differences between the He-rich and He-poor groups in this exercise.

The 2 μm feature. Although the overlaps between strong lines are less severe in the 2 μm region, the profile shapes of the 2 μm feature are not always well described by a single Gaussian function. A two-Gaussian fit was then chosen to determine the radial velocity shift. Note that for most spectra, there are two distinct features detected in the range of 1.95–2.15 μm. For each of these cases, the feature on the blue side is our target for fitting with the two-Gaussian function (dubbed the 2 μm feature), since it has been suggested in Section 5 that the feature on the red side may be attributed to Mg II λ2.1369 μm. In the case where the features are blended and indistinct, the velocity was then measured from the minimum of the entire profile. The results are represented in Figure 13.

Three lines are considered here for the identity of the 2 μm feature: He I λ2.0581 μm, C I λ2.1259 μm, and Mg II λ2.1369 μm (Figure 13). Assuming that the 2 μm feature is mainly formed by He I, the velocity ranges from approximately 5000–15,000 km s^{-1}. Assuming that the same feature is formed by C I and Mg II results in velocity ranges of 15,000–25,000 km s^{-1} and 17,000–27,000 km s^{-1}, respectively. Such high velocities for C I and Mg II are unlikely, especially when a feature to the red, often distinct from the 2 μm feature, yields reasonable velocity ranges of 3000–8000 and 5000–10,000 km s^{-1} for C I and Mg II, respectively.

Note that the He I velocities derived from the 2 μm feature are systematically lower than that indicated by the 1 μm feature. This apparent difference is expected if the 1 μm feature is formed at large optical depths, that tend to push the minimum toward the blue (Section 6.3). Similar to the result from the 1 μm feature, the 2 μm feature tends to be at redder wavelengths indicating lower velocities on average in the He-poor group compared to the He-rich group. Considering that SNe Ic/Ic-BL are on average more energetic events than SNe IIb/Ib, the 2 μm feature may not have been formed by the same lines in both groups.

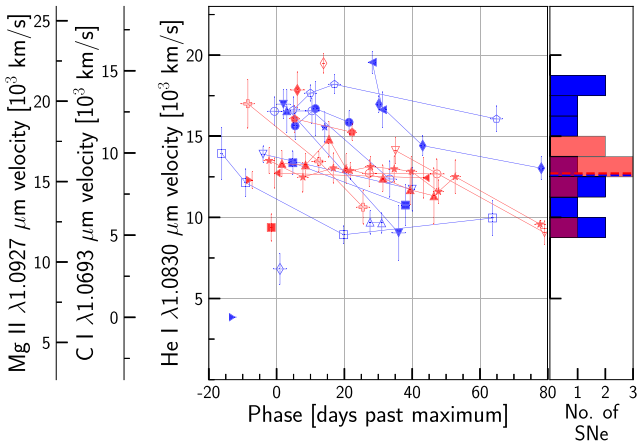

Figure 12. The velocity of the absorption feature at 1 μm, assuming that the two-Gaussian fitting function represents a single ion. The assumed ion is indicated for each panel on the *y*-axis. The same symbols from Figure 11 are used here. The histograms are shown for SNe with available velocity measurements interpolated to 30 days past maximum. The blue and red dashed lines on the histograms mark the median velocity for SNe IIb/Ib and SNe Ic/Ic-BL at day 30, respectively.

Both the pEW measurements (Section 4.1) and the PCA (Section 5) point to the 2 μm region as the ideal place to detect the presence of He. These analyses were able to distinguish NIR He-rich and He-poor groups that almost perfectly correspond to the optical IIb/Ib and Ic/Ic-BL designations, respectively. The examinations of the 2 μm observations also show that He-rich and He-poor SNe have distinct properties. Thus, based on our observations, the division between the two groups is not an arbitrary one along a continuous sequence. The NIR observations then lend credence to the optical Ib/Ic division.

6.2. Search for Residual He in He-poor SNe

We now turn to the question of whether He-poor SNe do in fact harbor trace amounts of He. In Figure 14, the 2 μm region

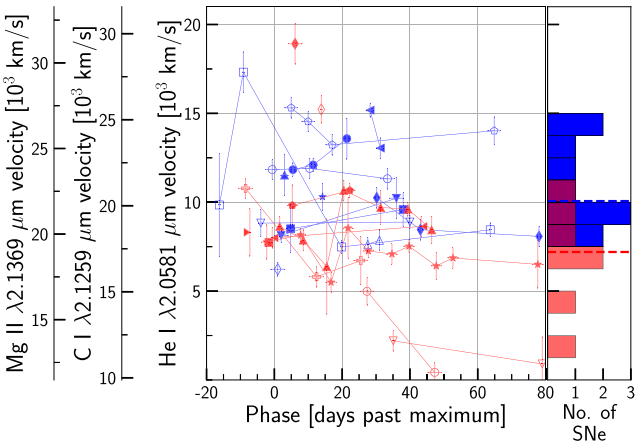

Figure 13. The velocity of the absorption feature at 2 μm measured by fitting a two-Gaussian function. The assumed ion is indicated for each panel on the *y*-axis. The same symbols from Figure 11 are used here. The histograms are shown for SNe with available velocity measurements interpolated to 30 days past maximum. The blue and red dashed lines on the histograms mark the median velocity for SNe IIb/Ib and SNe Ic/Ic-BL at day 30, respectively.

is presented for all the SN Ic spectra in our sample with a high enough S/N ratio in the *K* band. A significant fraction of the He-poor spectra in the sample show weak absorption features near 2 μm. In particular, SN 2013ge and SN 2014L, two of the best-sampled He-poor SNe, show varied time evolution and the persistence of this feature. Drout et al. (2016) identified the weak feature in SN 2013ge as He I λ2.0581 μm and proposed that the feature persists out to +40 days past maximum (black vertical line in Figure 14). It was then classified as a SN Ib/c by Drout et al. (2016) using the combination of the optical and NIR He lines. The evolution of He I λ2.0581 μm in SN 2014L is more complex, possibly showing two components emerging at different epochs (dashed and solid red vertical lines in Figure 14). The component indicated by the red dashed line in Figure 14 emerges later and continues to strengthen at late epochs. Indeed, this component may be formed by other ions, and the He I features in both SN 2013ge and SN 2014L may only persist to 1–2 weeks past maximum rather than >1 month as previously proposed. This could be due to the He layers becoming optically thin by these epochs.

Among the SNe Ic in our sample, SN 2014L, SN 2013ge, and SN 2012hf show evidence of trace amounts of He through the weak He I λ2.0581 μm absorption. However, the early and high S/N ratio spectra of SN 2014ar, SN 2013dk, and SN 2014eh can rule out the existence of He I λ2.0581 μm absorption. LSQ13doo does not have an early enough spectrum for this line to be ruled out. To summarize, even though the He I λ2.0581 μm absorption in SNe Ic is much weaker compared to SNe IIb/Ib, approximately half of the SNe Ic in our sample show a weak absorption. Although this is a significant fraction, we caution that our sample is in no way statistically complete or representative of the population in nature. As mentioned previously, the distinct feature to the red side near 2.1 μm and well separated from the He I complex may be attributed to C I λ2.1259 μm and/or Mg II λ2.1369 μm (purple vertical line in Figure 14).

6.3. Line Identifications Through Models

In this section, we use the models of Teffs et al. (2020) to compare with observations and guide us in line identifications.

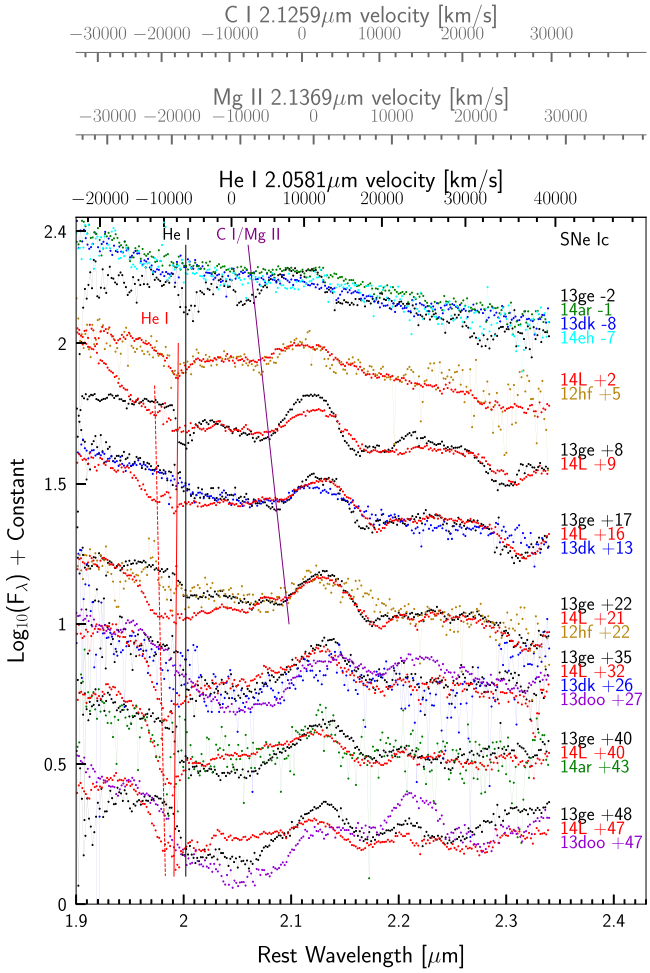

Figure 14. Spectral evolution of SNe Ic in the 2 μm region. The top *x*-axis shows the velocity scale of the He I λ2.0581 μm, Mg II λ2.1369 μm, and C I λ2.1259 μm lines. The vertical lines indicate possible He I evolution for SN 2013ge (black) and SN 2014L (red). There may be two components for SN 2014L (see text for details). The purple lines indicate a possible C I/Mg II feature. SNe Ic-BL have been excluded from this plot. The spectra of SN 2013co and LSQ13lo have also been excluded due to their low S/N ratios in the region.

This series of models are based on a 22 $M_\odot$ progenitor from Woosley et al. (2002), that is stripped of H/He in a successive method prior to collapse to produce a set of Type Ic/Ib/IIb-like models. These models are exploded at a variety of predefined final explosion energies and a mixing approximation is applied before a series of time-dependent spectra are calculated. For alternative models see Dessart et al. (2015, 2020). Figure 15 presents a selection of line identifications for a set of synthetic SNe IIb/Ib/Ic spectra at two epochs: 2 days prior and +21 days past peak luminosity. Details regarding the explosion models are given in Teffs et al. (2020).

For all models, we start with a 22 $M_\odot$ progenitor stripped of H/He of varying degrees prior to collapse. The SN IIb model is exploded at a final energy of 3 foe and ejects 5.8 $M_\odot$ of material comprised of an atmosphere of 0.1 $M_\odot$ of H and 1.3 $M_\odot$ of He above an evenly mixed C/O rich core. These mixing approximations result in the early spectral features forming primarily in the H/He-rich regions, thus containing minimal contributions from other elements such as O and Ca. By 21 days past maximum, the photosphere has receded into the C/O rich core, producing several of the C, O, Mg, and Fe-

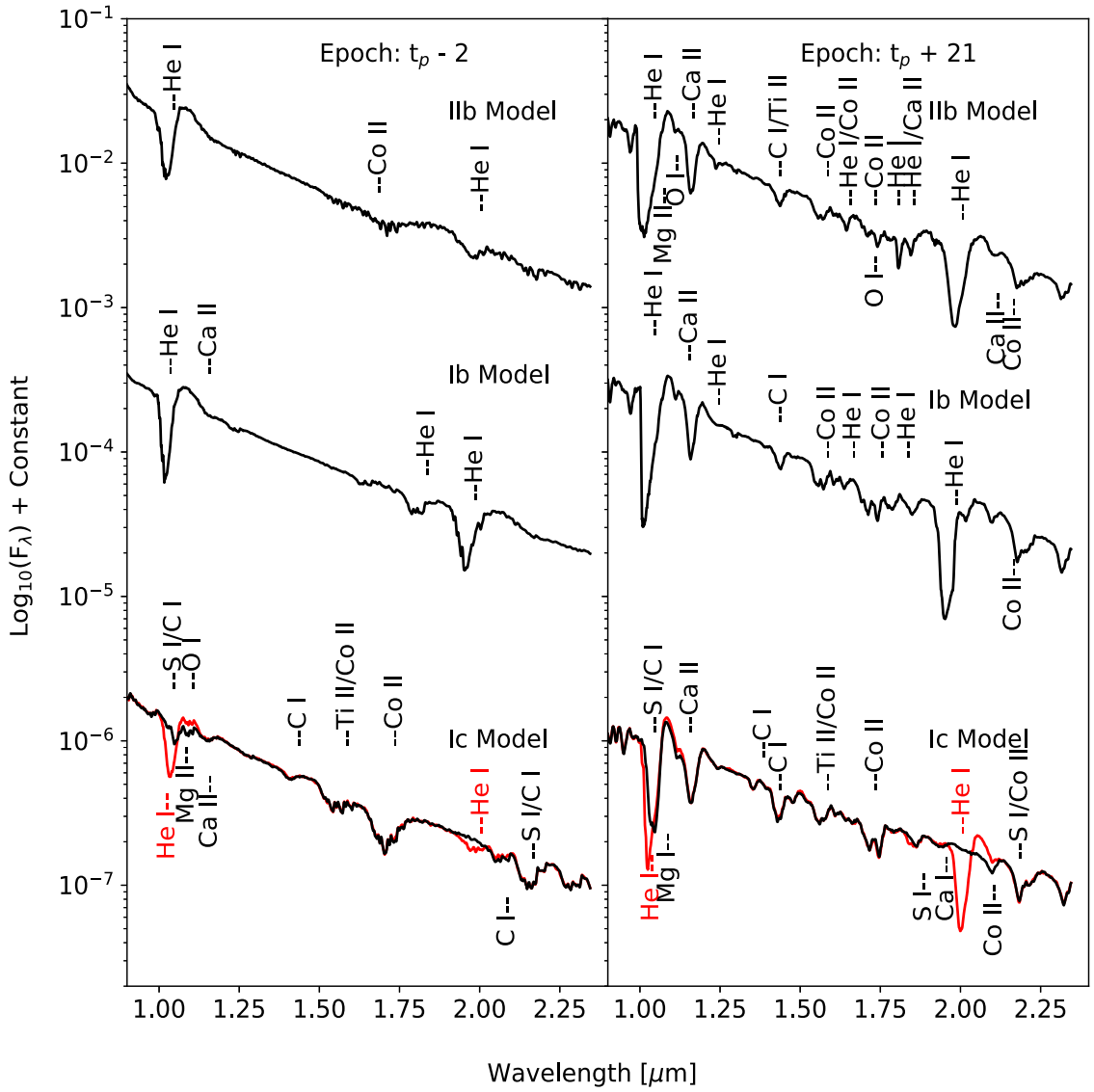

Figure 15. NIR line identifications based on a subset of synthetic spectra from Teffs et al. (2020). They are presented at two epochs: 2 days prior and +21 days past peak luminosity, plotted in the left and right panels, respectively. The SN IIb, Ib, and Ic model spectra are shown at each epoch. For the SN Ic model, the red spectra model has 0.02 $M_\odot$ of He mixed evenly through the C/O core while the black has no He mass in the model. The ions responsible for the absorption features are labeled. See text for the model properties.

group lines as identified in Section 3. The rich He shell is still the dominant line forming region, producing easily identifiable 1 and 2 μm lines.

The SN Ib model is also exploded at a final energy of 3 foe, and ejects 5.3 $M_\odot$ of material with 1.0 $M_\odot$ of He. This model uses a similar mixing approximation as the IIb model, with a He-rich shell above a mixed C/O core, and was shown in Teffs et al. (2020) to match several SNe Ib in the optical. Similar to the IIb model, at 2 days prior to peak luminosity, the photosphere is still in the He-rich outer shell. The apparent strength of the He I λ2.0581 μm line is stronger in the Ib model compared to that in the IIb, due to the relative abundances above each photosphere of H/He. By 21 days past maximum, the SN IIb and Ib synthetic spectra show few differences, as shown in the observed spectrum in the previous sections. The lack of the Paschen series in the NIR for our H-poor models results from effectively both the IIb/Ib having a C/O rich core below a He shell.

The SN Ic model is also exploded at a final energy of 3 foe, and ejects 4.2 $M_\odot$ of material with no He and is thoroughly mixed. A second SN Ic model, that shows minimal to no optical features, is included with 0.02 $M_\odot$ of He mixed throughout the ejecta. The spectrum of the He-free SN Ic model at 2 days before maximum shows no dominant line near 1 μm. Instead, the region is comprised of three weaker S I, C I, and Mg II lines that become significantly stronger with time. In the model with trace amounts of He, we find a strong absorption feature due to He I. Note however that the vast majority of SNe Ic in our observed sample exhibit the strong 1 μm absorption feature from the earliest phases. Based on the mixing approximation used, this may not place enough C, S, or Mg at higher velocities that would generate a dominant, non-He I feature at 1 μm.

Given the late-time dominance of the S I and C I lines of the 1 μm feature in the models, modification of outer abundance structure may still reproduce the observed early feature without

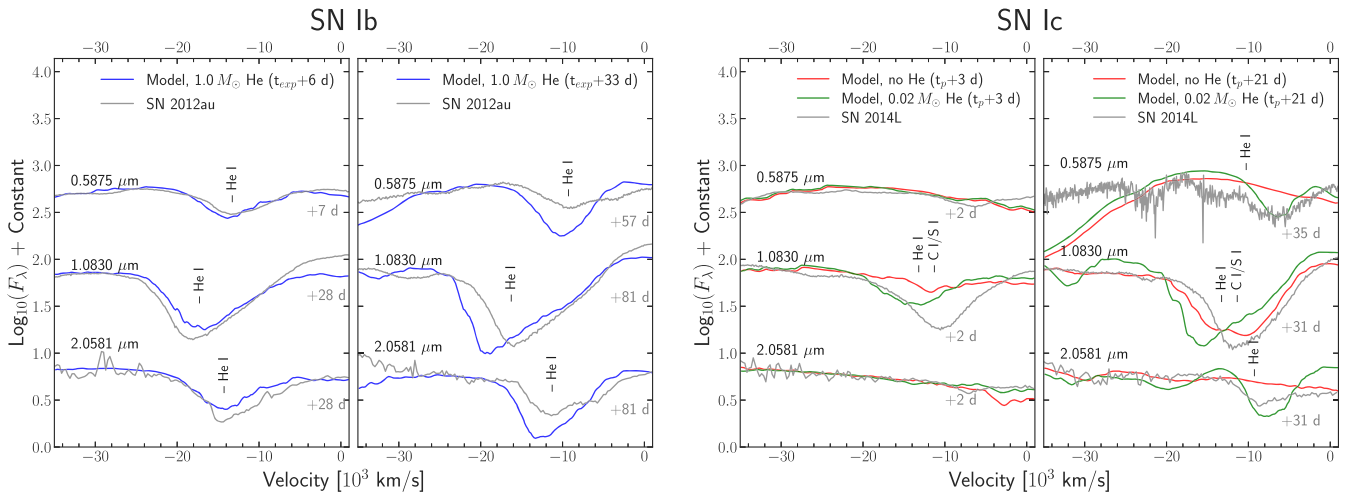

Figure 16. Comparison between observed spectra and the synthetic model spectra of Teffs et al. (2020) in the velocity space of He I. The observed optical and NIR spectra of Type Ib SN 2012au (left panel) and Type Ic SN 2014L (right panel) are shown in two epochs. They are compared to the SN Ib model (left panel) and the SN Ic model with a contribution of 0.02 $M_\odot$ of He I included (right panel).

the need for He. Additionally, the 1 μm feature in the later epoch is dominant in both models with little difference between the models with and without He. As the photosphere recedes in the C/O core for both epochs, the spectra show much stronger Ca II and C I lines than in the SN Ib model. The strong Ca II λ1.1839 μm and λ1.1950 μm lines are also present in the observed SN Ic spectra. Consistent with observations, the largest difference between the He-rich SN IIb/Ib and the He-poor SN Ic models is in the 2 μm feature where the He-rich models are dominated by the He I λ2.0581 μm line.

One prevalent ion in all of the synthetic spectra is Co II. The features formed by Co II may be a consequence of the mixing approximations for ^{56}Ni chosen in these models. It is unclear whether they are present in the observed spectra. The ^{56}Ni distribution in the SN IIb/Ib models assumes a central mass of ^{56}Ni that has a running boxcar average across the ejecta, resulting in a relatively smooth decrease in the abundance of ^{56}Ni outside the core. The SN Ic model, however, has an even distribution of ^{56}Ni throughout the ejecta and the over-abundance of ^{56}Ni in the outermost region may result in stronger Co II features in the synthetic spectra.

In the left panel of Figure 16, the observed spectra of Type Ib SN 2012au and the synthetic spectra of the SN Ib model described above are compared in the velocity space of He I at two epochs and for the three strongest He I lines: λ0.5875 μm, λ1.0830 μm, and λ2.0581 μm. The model can largely reproduce the observed velocity and profile shape. Minor mismatches at later phases may be attributed to the differences in epochs, densities, and ionization/excitation regimes. Most notably, both the 1 μm and 2 μm features can easily be dominated by minimal to moderate amounts of He, resulting in broadened wings. This explains the observed asymmetric profile shapes and highlights the difficulty in determining the velocity using these features.

In the right panel of Figure 16, the observed spectra of Type Ic SN 2014L are compared to the synthetic spectra of the SN Ic model in the velocity space of He I. For this comparison, 0.02 $M_\odot$ of He is included in the SN Ic model. If He contributes to all three features in the three wavelength regions, then the velocity appears to be consistent. Note that it is always difficult to rule out Na I D being the dominant species in the optical region. The match in the 2 μm region at the later epoch is substantially improved by the addition of the trace amount of He. This result is consistent with our finding that some SNe Ic in our sample harbor small amounts of He (Section 6.2). The optical feature in SN 2014L may be improved simply by introducing Na into the model, which is an element not included in the models in Teffs et al. (2020). However, caution should be taken from these comparisons. The flux for both synthetic and observed SNe are scaled or normalized and are not given in absolute flux values. The luminosity and photospheric temperature required to reproduce the observed flux level in the SN may not be the same parameters used to calculate the synthetic spectra. Furthermore, Teffs et al. (2020) showed that for SNe Ic, the completely mixed C/O core was successful in reproducing the observed behavior of several observed SNe. However, SNe Ic are directly modeled using the abundance tomography method, such as SN 2004aw (Mazzali et al. 2017), SN 1994I (Sauer et al. 2006), and SN 2017ein (Teffs et al. 2021), require varied abundance distributions in order to reproduce the observed spectra. A proper abundance stratification model following the methods in Stehle et al. (2005) and Ashall et al. (2019) would be required to determine if SN 2014L has He in the ejecta but is beyond the scope of this work.

7. Conclusions

We have presented the largest NIR spectroscopic data set of SESNe to date, which encompasses 75 NIR spectra of 34 SESNe observed by CSP-II between 2011 and 2015. The spectra past 80 days relative to maximum are excluded from this paper and will be discussed in a following paper that mostly focuses on the detection of CO.

Our main findings for this work are summarized as follows:

(1) All spectra, regardless of their optical classification, show a broad and strong absorption profile at around 1 μm. There are multiple strong lines in this region that may be responsible for this feature, complicating the analysis. These include: He I λ1.0830 μm, C I λ1.0693 μm and Mg II λ1.0927 μm. In SNe Ib and IIb, the He I line is likely to be the main contributor to this feature. In SNe Ic and Ic-BL, the presence of other C I and Mg II lines in the spectra suggests the possibility of line blending for the 1 μm feature. These complications motivated us to investigate the 2μm region.

(2) Our sample of SESNe show two distinct groups based on their NIR properties. These groups are dubbed NIR "He-rich" and "He-poor" and correspond almost perfectly to the optical SN IIb/Ib and SN Ic/Ic-BL groups, respectively. Both the pEW and the PCA measurements show a dichotomy between the He-poor and He-rich groups (Figures 6 and 9). The dichotomy demonstrates that the 2 μm region is the ideal place to detect the presence of He.

(3) Our investigations on the 2 μm region suggest that there are some trace amounts of He detected at early times in some He-poor SNe, confirming the results from previous works (e.g., Wheeler et al. 1994; Filippenko et al. 1995; Clocchiatti et al. 1996; Hachinger et al. 2012; Piro & Morozova 2014; Drout et al. 2016; Prentice et al. 2018). Even though the He I λ2.0581 μm absorption in the He-poor SNe is much weaker compared to the He-rich, approximately half of the He-poor SNe in our sample show weak absorption features from this line. Thus, there is perhaps some He I contribution to the 1 μm feature in these SNe as well.

There are many ways that SESNe can lose their outer envelopes, including eruptions, radiation-driven winds, stripping from a common envelope in a binary system, fast rotations in Be stars, or a combination of them. One may expect that if the mass loss is from a single process, it would manifest as a continuous range of observed properties, indicating the degree of envelope stripping. NIR spectra provide a unique route to observe this, especially given the differences in the residual He. In this work, we find an abrupt difference in the 2 μm region between He-poor and He-rich SNe in our spectral and PCA analyses. This may indicate distinct mass-loss mechanisms for He-poor and He-rich SNe. It may also be possible for a single mechanism to produce very different observational properties. Further theoretical studies are therefore needed. For instance, the He shell and core mass may be estimated by comparing NIR observations and models. Coupling this with stellar evolution information can place further constraints on the progenitor systems and the explosion mechanisms.

We are pleased to acknowledge the following individuals (in alphabetical order) for their assistance in obtaining the NIR spectroscopic data set: Y. Beletsky, T. Dupuy, R. Foley, L. W. Hsiao. We also thank the Las Campanas Observatory technical staff for their continued support over the years. The CSP-II has been supported by NSF grant Nos. AST-1008343, AST-1613426, AST-1613455, and AST-1613472. C.A. is supported by NASA grant No. 80NSSC19K1717 and NSF grant Nos. AST-1920392 and AST-1911074. J.T. is funded by the consolidated STFC grant No. R276106. L.G. acknowledges financial support from the Spanish Ministry of Science, Innovation and Universities (MICIU) under the 2019 Ramón y Cajal program RYC2019-027683 and from the Spanish MICIU project PID2020-115253GA-I00. C.G. is supported by a Young Investor Grant (25501) from the VILLUM FONDEN. Time domain research by D.J.S. is also supported by NSF grant Nos. AST-1821987, 1813466, 1908972, & 2108032, and by the Heising-Simons Foundation under grant #2020-1864. M. D.S. is supported by grants from the VILLUM FONDEN (grant No. 28021) and the Independent Research Fund Denmark (IRFD; 8021-00170B).

Software: `firehose` (Simcoe et al. 2013), `SNID` (Blondin & Tonry 2007), `SNooPy` (Burns et al. 2011), `xtellcor` (Vacca et al. 2003).

Appendix A
Classification

The optical classifications used in this work are listed in Table A1 in comparison to the previously published ones. The sources of optical spectra used are also listed. For each SN, the spectrum closest to maximum light was selected if it has an adequate S/N ratio for classification. The package SNID with the updated templates from Liu & Modjaz (2014) was then used for the classification. Only slight differences were found comparing the classifications of this work with the previously reported ones. There were no SNe that changed between the IIb/Ib and Ic/Ic-BL groups. Table A2 lists all the SESNe in the sample that were classified using FIRE. Note that in the NIR, it is difficult to distinguish between SNe IIb and Ib.

Table A1
Optical Spectroscopic Classification

SN	Optical Classification		Source of Optical Spectrum	
	Published	This work[a]	Published	This work
ASASSN-14az	IIb	IIb	Benetti et al. (2014)	Shivvers et al. (2019)
LSQ13abf	Ib	Ib	Stritzinger et al. (2020)	CSP
LSQ13cum	Ib	Ib	Taddia et al. (2013)	CSP
LSQ13ddu	Ibn	Ibn	Clark et al. (2020)	CSP
LSQ13doo	Ic-BL	Ic/Ic-BL	Bersier et al. (2013)	PESSTO
LSQ13lo	Ib/c	Ic	Hadjiyska et al. (2013)	CSP
LSQ14akx	IIb	IIb	Taddia et al. (2014)	CSP
OGLE-2014-SN-067	Ic	Ic-BL	Childress et al. (2014)	Childress et al. (2016)
iPTF13bvn	Ib	Ib	Fremling et al. (2016)	Cao et al. (2013)
SN 2011hs	IIb	IIb	Bufano et al. (2014)	CSP
SN 2012J	Ib/c	Ic	Monard et al. (2012)	CSP
SN 2012P	IIb	IIb	Fremling et al. (2016)	Fremling et al. (2016)
SN 2012ap	Ic-BL	Ic-BL	Milisavljevic et al. (2015)	CSP
SN 2012au	Ib	Ib	Milisavljevic et al. (2013)	Milisavljevic et al. (2013)
SN 2012hf	Ic	Ic	Hamuy et al. (2012)	PESSTO
SN 2012hn	Ic	Ic	Howerton et al. (2012)	PESSTO
SN 2013ak	IIb	IIb	Milisavljevic et al. (2013)	CSP
SN 2013co	Ic-BL	Ic	Zhang et al. (2013)	Zhang et al. (2013)
SN 2013dk	Ic	Ic	Carrasco et al. (2013)	Elias-Rosa et al. (2013)
SN 2013ek	Ib	Ib	Valenti et al. (2013)	PESSTO
SN 2013el	Ib-pec	IIb	Valenti et al. (2013)	Shivvers et al. (2019)
SN 2013fq	Ib	IIb	Hsiao et al. (2013)	Childress et al. (2016)
SN 2013ge	Ib/c	Ic	Drout et al. (2016)	Drout et al. (2016)
SN 2014L	Ic	Ic	Zhang et al. (2018)	CSP
SN 2014ad	Ic-BL	Ic-BL	Stevance et al. (2017)	PESSTO
SN 2014ar	Ic	Ic	Morrell et al. (2014)	CSP
SN 2014cp	Ic-BL	Ic-BL	Childress et al. (2014)	Childress et al. (2016)
SN 2014df	Ib	Ib	Childress et al. (2014)	Childress et al. (2016)
SN 2014eh	Ic	Ic	Hosseinzadeh et al. (2014)	PESSTO
SN 2015Y	IIb	Ib	Childress et al. (2015)	Shivvers et al. (2019)

Table A2
FIRE NIR Spectroscopic Classifications of SESNe

SN	Source of Classification
LSQ12fwb	Hadjiyska et al. (2012)
LSQ13lo	Hadjiyska et al. (2013)
OGLE-2013-SN-134	Hsiao et al. (2013)
OGLE-2014-SN-014	Marion et al. (2014)
PSN J11220840-3804001	Marion et al. (2014)
SN 2013ak	Milisavljevic et al. (2013)
SN 2013dk	Marion et al. (2013)
SN 2013fq	Hsiao et al. (2013)
SN 2014df	Marion et al. (2014); Morrell et al. (2014)

Appendix B
Spectra Excluded from Analyses

In this section, we list the eight NIR spectra of eight SESNe excluded from our analyses, either because they do not have reliable phase estimates or optical spectroscopic classifications (Table B1). These SNe are presented in Figure B1.

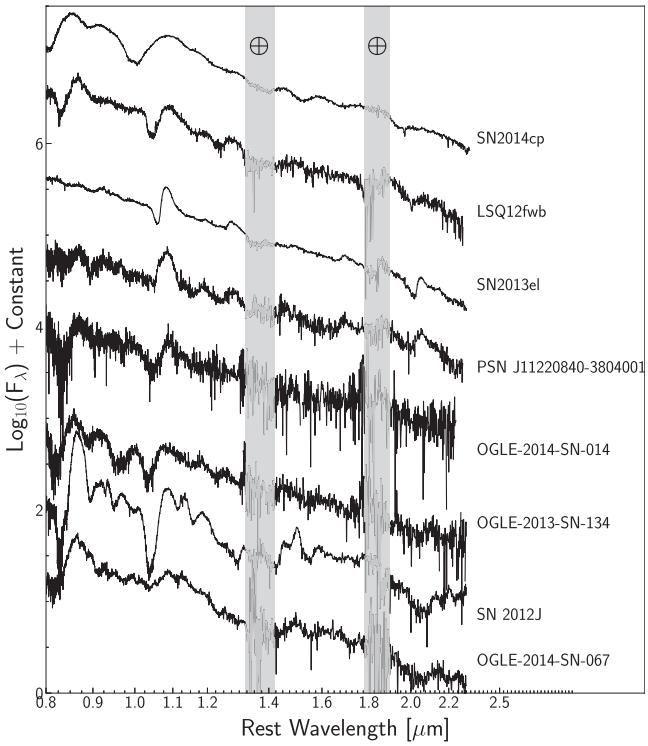

Figure B1. Spectra of SNe with only one spectrum within the sample that do not have optical spectra and reliable photometry available.

Table B1
SNe with No Reliable Phase or Optical Spectroscopic Classification

SN[a]	Host	Redshift	UT Date	MJD$_{obs}$	Telluric STD	Airmass
LSQ12fwb	CGCG 409-012	0.0298	2012-11-05	56236.6	HD8325	1.26
OGLE-2013-SN-134	WISEA J061355.87-725821.1	0.0382	2013-12-14	56640.7	HD19839	1.39
OGLE-2014-SN-014	WISEA J042722.73-744206.6	0.0430[b]	2014-02-15	56703.5	HD26493	1.45
OGLE-2014-SN-067	Anonymous	0.0187	2014-09-03	56903.9	HD42651	1.48
PSN J11220840-3804001	ESO 319- G 016	0.0096	2014-06-06	56814.6	HD100852	1.33
SN 2012J	ESO 386-IG 039	0.0094	2012-02-03	55960.8	HD125062	1.52
SN 2013el	NGC 1285	0.0175	2013-07-16	56489.9	HD25266	1.27
SN 2014cp	ESO 479- G 001	0.0162	2014-07-10	56848.9	HD16636	1.22

Note.
[a] Redshift obtained from Marion et al. (2014).

Appendix C
Notable Objects

SN 2014df. SN 2014df has an unusual feature at $\sim$2 μm, shown in Figure 3, that makes investigating this SN interesting. This feature at $\sim$2 μm shows two components in the earliest spectrum. This two-component feature reverts to a single apparent component in the subsequent spectrum, taken 52 days afterward. SN 2014df is the only SN in this sample that shows this unusual double component feature. In order to identify this feature, we measured the He I velocity of the blue component of this feature to be at 14,400 km s^{-1} and the red component to be 8200 km s^{-1}. Assuming Mg II the blue component gives a velocity of 24,900 km s^{-1}, and the red component gives 19,000 km s^{-1}. Since we observe a really high velocity by assuming Mg II, it is unlikely that either of these two components are formed by Mg II. Therefore, both components could possibly be a result of He I with one of the components formed by high-velocity He I.

PSN J11220840-3804001. It is worth noting that, there is one SN in the sample, PSN J11220840-3804001, that has a very similar spectrum to the NIR spectra of LSQ13ddu. Clark et al. (2020) classified LSQ13ddu as a SN Ibn. Figure C1 compares the two SNe with some of the features identified.

Appendix D
Gaussian Fits

Figures C2 and C3 present the Gaussian fits done to measure velocities.

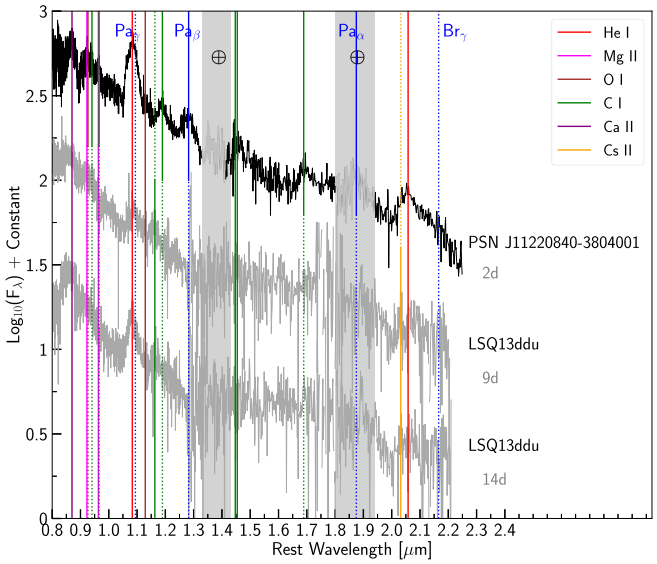

Figure C1. Comparing spectra of PSN J11220840-3804001 with LSQ13ddu. PSN J11220840-3804001 is plotted in black and LSQ13ddu with two spectra is plotted in gray.

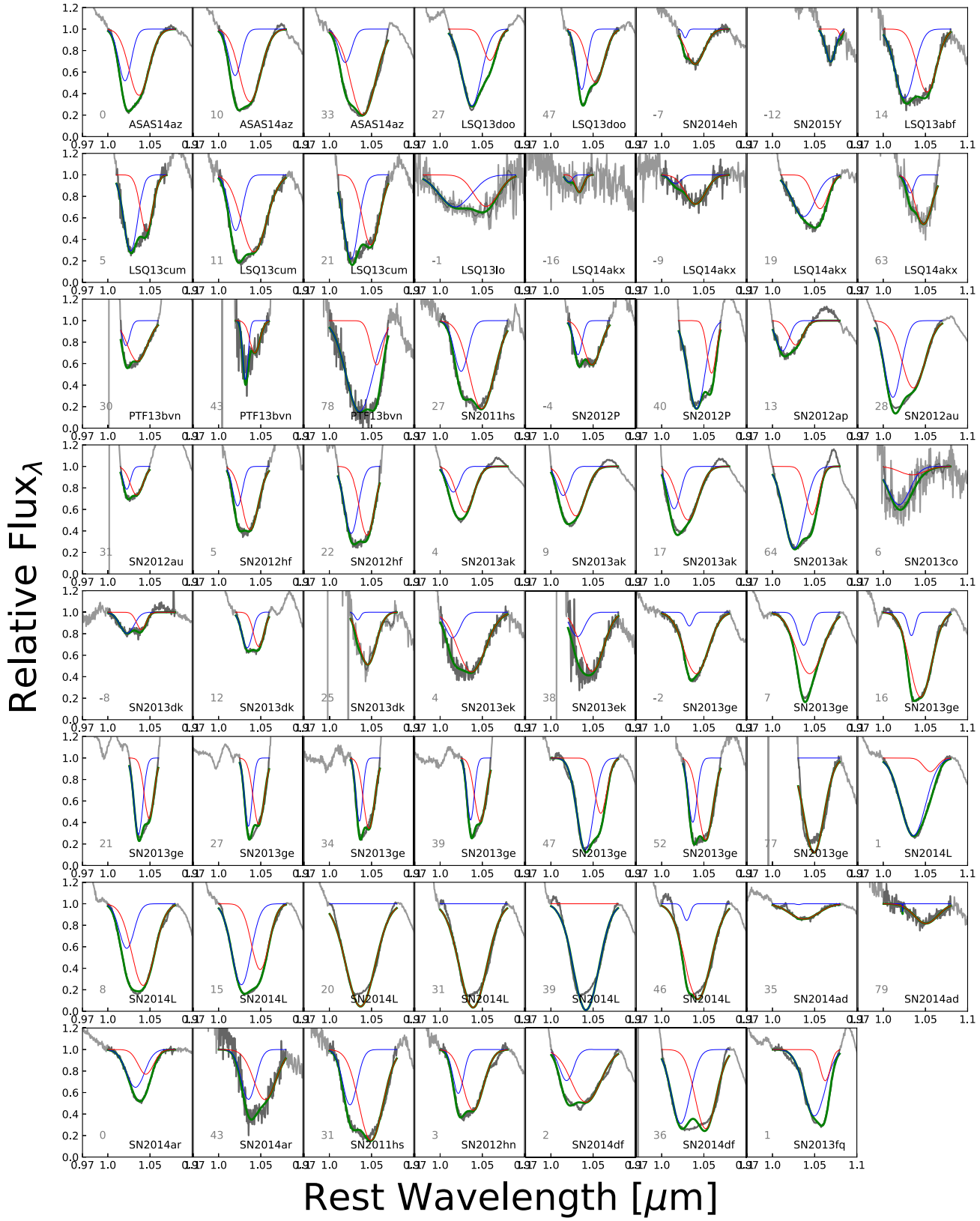

Figure C2. The two-Gaussian fits for the 1 μm region of all the spectra used in the analysis. The two earliest spectra of SN 2014ad were excluded due to the fact that there is not a strong enough feature in these two spectra to fit. LSQ13ddu was excluded due to low S/N ratio. For cases that a minimum was not found for one of the components, the minimum of the entire feature was considered for that component instead (Figure 11).

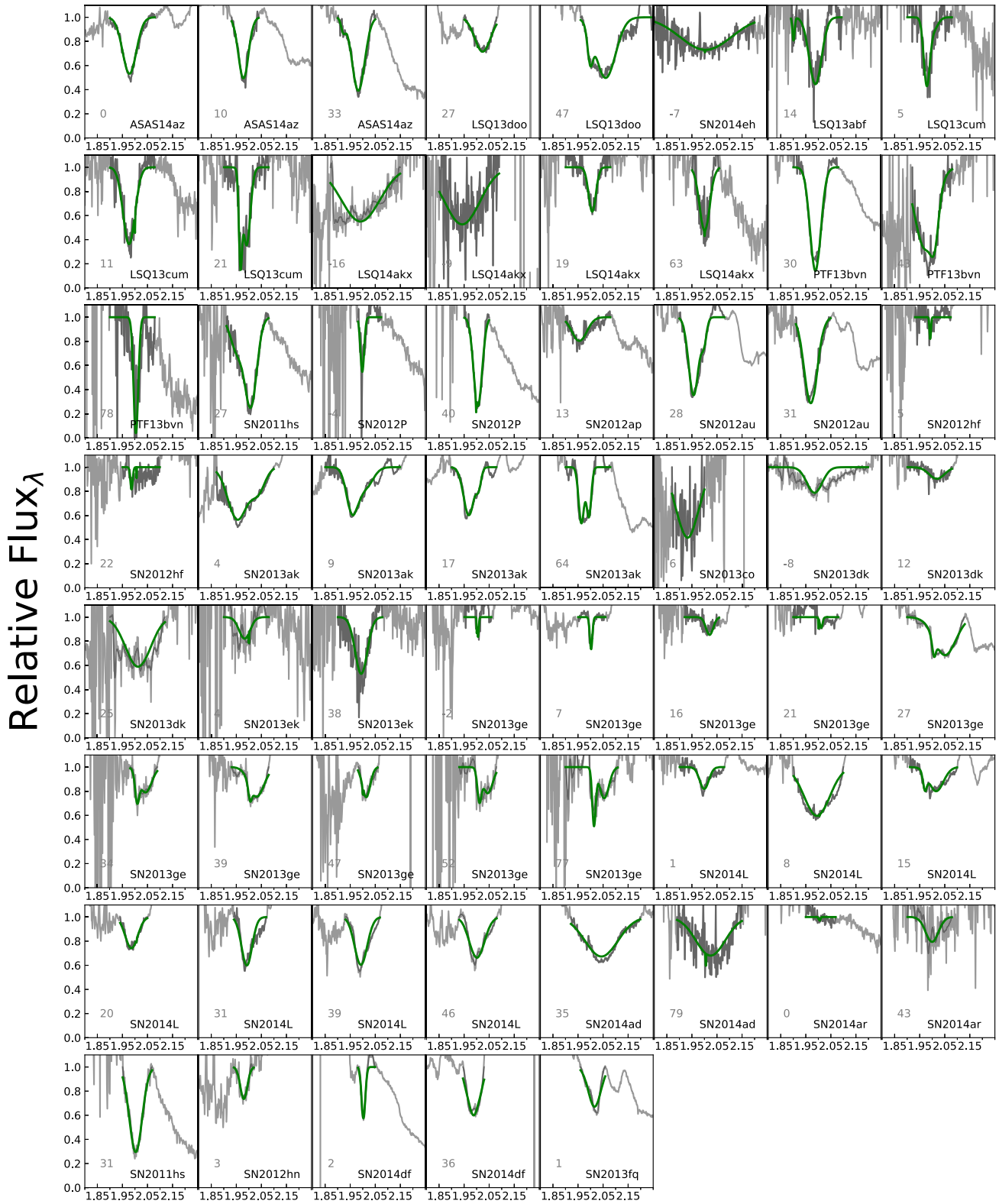

Figure C3. The two-Gaussian fits for the 2 μm region of all the spectra used in the analysis. The two earliest spectra of SN 2014ad were excluded due to the fact that there is not a strong enough feature in these spectra to fit. The SNe with S/N ratio lower than 5 in the 2 μm region were also excluded. Since we did not measure and use the minimum of each component individually for this feature, the two Gaussian components are not shown.

ORCID iDs

M. Shahbandeh https://orcid.org/0000-0002-9301-5302
E. Y. Hsiao https://orcid.org/0000-0003-1039-2928
C. Ashall https://orcid.org/0000-0002-5221-7557
J. Teffs https://orcid.org/0000-0001-8290-2881
P. Hoeflich https://orcid.org/0000-0002-4338-6586
N. Morrell https://orcid.org/0000-0003-2535-3091
M. M. Phillips https://orcid.org/0000-0003-2734-0796
J. P. Anderson https://orcid.org/0000-0003-0227-3451
E. Baron https://orcid.org/0000-0001-5393-1608
C. R. Burns https://orcid.org/0000-0003-4625-6629
C. Contreras https://orcid.org/0000-0001-6293-9062
S. Davis https://orcid.org/0000-0002-2806-5821
T. R. Diamond https://orcid.org/0000-0002-0805-1908
G. Folatelli https://orcid.org/0000-0001-5247-1486
L. Galbany https://orcid.org/0000-0002-1296-6887
C. Gall https://orcid.org/0000-0002-8526-3963
S. Hachinger https://orcid.org/0000-0001-8341-1478
S. Holmbo https://orcid.org/0000-0002-3415-322X
E. Karamehmetoglu https://orcid.org/0000-0001-6209-838X
M. M. Kasliwal https://orcid.org/0000-0002-5619-4938
R. P. Kirshner https://orcid.org/0000-0002-1966-3942
K. Krisciunas https://orcid.org/0000-0002-6650-694X
S. Kumar https://orcid.org/0000-0001-8367-7591
J. Lu https://orcid.org/0000-0002-3900-1452
P. A. Mazzali https://orcid.org/0000-0001-6876-8284
A. L. Piro https://orcid.org/0000-0001-6806-0673
D. J. Sand https://orcid.org/0000-0003-4102-380X
M. D. Stritzinger https://orcid.org/0000-0002-5571-1833
N. B. Suntzeff https://orcid.org/0000-0002-8102-181X
F. Taddia https://orcid.org/0000-0002-2387-6801
S. A. Uddin https://orcid.org/0000-0002-9413-4186

References

Aldering, G., Humphreys, R. M., & Richmond, M. 1994, AJ, 107, 662
Ashall, C., Mazzali, P. A., Pian, E., et al. 2019, MNRAS, 487, 5824
Baltay, C., Rabinowitz, D., Hadjiyska, E., et al. 2013, PASP, 125, 683
Beasor, E. R., Davies, B., & Smith, N. 2021, ApJ, 922, 55
Benetti, S., Pastorello, A., Elias-Rosa, N., et al. 2014, ATel, 6185, 1
Bersier, D., Dennefeld, M., Lyman, J., et al. 2013, ATel, 5615
Bersten, M. C., Benvenuto, O. G., Folatelli, G., et al. 2014, AJ, 148, 68
Bersten, M. C., Benvenuto, O. G., Nomoto, K., et al. 2012, ApJ, 757, 31
Blondin, S., & Tonry, J. L. 2007, ApJ, 666, 1024
Bufano, F., Pignata, G., Bersten, M., et al. 2014, MNRAS, 439, 1807
Burns, C. R., Stritzinger, M., Phillips, M. M., et al. 2011, AJ, 141, 19
Cao, Y., Kasliwal, M. M., Arcavi, I., et al. 2013, ApJL, 775, L7
Carrasco, F., Hamuy, M., Antezana, R., et al. 2013, CBET, 3565, 1
Childress, M., Fogarty, L., Owers, M., et al. 2014, ATel, 6430
Childress, M., Scalzo, R., Yuan, F., et al. 2014, ATel, 6302
Childress, M., Scalzo, R., Yuan, F., et al. 2015, ATel, 7368
Childress, M., Zhou, G., Scalzo, R., et al. 2014, ATel, 6201
Childress, M. J., Tucker, B. E., Yuan, F., et al. 2016, PASA, 33, e055
Clark, P., Maguire, K., Inserra, C., et al. 2020, MNRAS, 492, 2208
Clocchiatti, A., Wheeler, J. C., Benetti, S., & Frueh, M. 1996, ApJ, 459, 547
Clocchiatti, A., Wheeler, J. C., Brotherton, M. S., et al. 1996, ApJ, 462, 462
Cohen, J. G., Darling, J., & Porter, A. 1995, AJ, 110, 308
Crowther, P. A. 2007, ARA&A, 45, 177
Crowther, P. A., Hadfield, L. J., Clark, J. S., et al. 2006, MNRAS, 372, 1407
Davis, S., Hsiao, E. Y., Ashall, C., et al. 2019, ApJ, 887, 4
Dessart, L., Hillier, D. J., Livne, E., et al. 2011, MNRAS, 414, 2985
Dessart, L., Hillier, D. J., Woosley, S., et al. 2015, MNRAS, 453, 2189
Dessart, L., Yoon, S.-C., Aguilera-Dena, D. R., et al. 2020, A&A, 642, A106
Djorgovski, S. G., Drake, A. J., Mahabal, A. A., et al. 2011, arXiv:1102.5004
Drout, M. R., Milisavljevic, D., Parrent, J., et al. 2016, ApJ, 821, 57
Elias-Rosa, N., Pastorello, A., Maund, J. R., et al. 2013, MNRAS, 436, L109
Ergon, M., Jerkstrand, A., Sollerman, J., et al. 2015, A&A, 580, A142
Filippenko, A. V., Barth, A. J., Matheson, T., et al. 1995, ApJL, 450, L11
Folatelli, G. 2004, NewAR, 48, 623
Folatelli, G., Van Dyk, S. D., Kuncarayakti, H., et al. 2016, ApJL, 825, L22
Fremling, C., Sollerman, J., Taddia, F., et al. 2014, A&A, 565, A114
Fremling, C., Sollerman, J., Taddia, F., et al. 2016, A&A, 593, A68
Gal-Yam, A. 2017, Handbook of Supernovae (Cham: Springer), p 195
Garavini, G., Folatelli, G., Nobili, S., et al. 2007, A&A, 470, 411
Hachinger, S., Mazzali, P. A., Taubenberger, S., et al. 2012, MNRAS, 422, 70
Hadjiyska, E., Walker, E., Rabinowitz, D., et al. 2012, ATel, 4563
Hadjiyska, E., Walker, E. S., Rabinowitz, D., et al. 2013, ATel, 4916
Hamuy, M., Antezana, R., Gonzalez, L., et al. 2012, CBET, 3326, 1
Heger, A., Fryer, C. L., Woosley, S. E., et al. 2003b, ApJ, 591, 288
Heger, A., Woosley, S. E., Fryer, C. L., & Langer, N. 2003a, Proc. of ESO/MPA/MPE Workshop, ed. W. Hillebrandt & B. Leibundgut, (Heidelberg: Springer), 3
Holoien, T. W.-S., Brown, J. S., Stanek, K. Z., et al. 2017, MNRAS, 471, 4966
Hosseinzadeh, G., Valenti, S., Arcavi, I., et al. 2014, ATel, 6667
Howerton, S., Drake, A. J., Djorgovski, S. G., et al. 2012, CBET, 3337, 1
Hsiao, E. Y., Conley, A., Howell, D. A., et al. 2007, ApJ, 663, 1187
Hsiao, E. Y., Marion, G. H., Beletsky, Y., Parker, S., & Phillips, M. M. 2013, ATel, 5400
Hsiao, E. Y., Marion, G. H., Morrell, N., et al. 2013, ATel, 5664
Hsiao, E. Y., Phillips, M. M., Marion, G. H., et al. 2019, PASP, 131, 014002
Iwamoto, K., Mazzali, P. A., Nomoto, K., et al. 1998, Natur, 395, 672
Kogure, T., & Hirata, R. 1982, BASI, 10, 281
Kuncarayakti, H., Maeda, K., Bersten, M. C., et al. 2015, A&A, 579, A95
Law, N. M., Kulkarni, S. R., Dekany, R. G., et al. 2009, PASP, 121, 1395
Leys, C., Klein, O., Bernard, P., & Licata, L. 2013, J. Exp. Soc. Psychol., 49, 764
Li, W. 2008, ATel, 1433
Liu, Y., & Modjaz, M. 2014, arXiv:1405.1437
Liu, Y.-Q., Modjaz, M., Bianco, F. B., et al. 2016, ApJ, 827, 90
Lucy, L. B. 1991, ApJ, 383, 308
Marion, G. H., Holmbo, S., Wyrzykowski, L., et al. 2014, ATel, 5891
Marion, G. H., Hsiao, E. Y., Gall, C., et al. 2014, ATel, 6220
Marion, G. H., Hsiao, E. Y., Roth, M., et al. 2013, ATel, 5167
Massa, D. 1975, PASP, 87, 777
Matheson, T., Filippenko, A. V., Li, W., et al. 2001, AJ, 121, 1648
Maund, J. R., Fraser, M., Ergon, M., et al. 2011, ApJL, 739, L37
Mazzali, P. A., Maurer, I., Valenti, S., et al. 2010, MNRAS, 408, 87
Mazzali, P. A., Sauer, D. N., Pian, E., et al. 2017, MNRAS, 469, 2498
Meynet, G., Hirschi, R., & Maeder, A. 2005, 1604-2004: Supernovae as Cosmological Lighthouses, 99
Meynet, G., & Maeder, A. 2005, A&A, 429, 581
Milisavljevic, D., Margutti, R., Parrent, J. T., et al. 2015, ApJ, 799, 51
Milisavljevic, D., Marion, G. H., Hsiao, E. Y., et al. 2013, ATel, 4943
Milisavljevic, D., Soderberg, A. M., Margutti, R., et al. 2013, ApJL, 770, L38
Monard, L. A. G., Sanders, N. E., Milisavljevic, D., et al. 2012, CBET, 2986, 1
Morrell, N., Hsiao, E. Y., Phillips, M., et al. 2014, ATel, 6082
Morrell, N., Marion, G. H., Kirshner, R. P., et al. 2014, ATel, 6442
Newville, M., Stensitzki, T., Allen, D. B., et al. 2014, LMFIT: Non-Linear Least-Square Minimization and Curve-Fitting for Python v0.8.0, Zenodo, doi:10.5281/zenodo.11813
Nomoto, K. 1984, ApJ, 277, 791
Nomoto, K. 1987, ApJ, 322, 206
Owocki, S. 2006, ASP Conf. Ser. 355, Stars with the B[e] Phenomenon ed. A. Meilland, M. Kraus, & A. S. Miroshnichenko, (San Francisco, CA: ASP), 219
Parker, S., Kiyota, S., Brimacombe, J., et al. 2013, CBET, 3665
Pauldrach, A. W. A., Vanbeveren, D., & Hoffmann, T. L. 2012, A&A, 538, A75
Pessi, P. J., Folatelli, G., Anderson, J. P., et al. 2019, MNRAS, 488, 4239
Phillips, M. M., Contreras, C., Hsiao, E. Y., et al. 2019, PASP, 131, 014001
Piro, A. L., & Morozova, V. S. 2014, ApJL, 792, L11
Podsiadlowski, P., Hsu, J. J. L., Joss, P. C., et al. 1993, Natur, 364, 509
Podsiadlowski, P., Langer, N., Poelarends, A. J. T., et al. 2004, ApJ, 612, 1044
Pols, O. R., & Dewi, J. D. M. 2002, PASA, 19, 233
Prentice, S. J., Ashall, C., Mazzali, P. A., et al. 2018, MNRAS, 478, 4162
Rho, J., Evans, A., Geballe, T. R., et al. 2021, ApJ, 908, 232
Rousseeuw, P. J., & Croux, C. 1993, J. Am. Stat. Assoc., 88, 1273
Sahu, D. K., Anupama, G. C., Chakradhari, N. K., et al. 2018, MNRAS, 475, 2591
Sauer, D. N., Mazzali, P. A., Deng, J., et al. 2006, MNRAS, 369, 1939
Shappee, B., Prieto, J., Stanek, K. Z., et al. 2014, AAS Meeting Abstracts, 223, 236.03
Shivvers, I., Filippenko, A. V., Silverman, J. M., et al. 2019, MNRAS, 482, 1545

Simcoe, R. A., Burgasser, A. J., Schechter, P. L., et al. 2013, PASP, 125, 270
Slettebak, A. 1988, PASP, 100, 770
Smith, N. 2006, arXiv:astro-ph/0607457
Smith, N., & Owocki, S. P. 2006, ApJL, 645, L45
Stehle, M., Mazzali, P. A., Benetti, S., et al. 2005, MNRAS, 360, 1231
Stevance, H. F., Maund, J. R., Baade, D., et al. 2017, MNRAS, 469, 1897
Stritzinger, M. D., Taddia, F., Holmbo, S., et al. 2020, A&A, 634, A21
Taddia, F., Stritzinger, M., Morrell, N., et al. 2013, ATel, 5561
Taddia, F., Stritzinger, M., Morrell, N., et al. 2014, ATel, 5998
Taubenberger, S., Navasardyan, H., Maurer, J. I., et al. 2011, MNRAS, 413, 2140
Taubenberger, S., Pastorello, A., Mazzali, P. A., et al. 2006, MNRAS, 371, 1459
Teffs, J., Ertl, T., Mazzali, P., et al. 2020, MNRAS, 492, 4369
Teffs, J. J., Prentice, S. J., Mazzali, P. A., et al. 2021, MNRAS, 502, 3829
Vacca, W. D., Cushing, M. C., & Rayner, J. T. 2003, PASP, 115, 389
Valenti, S., Graham, M. L., Howell, D. A., Sand, D., & Parrent, J. T. 2013, ATel, 5206
Valenti, S., Sand, D., Howell, D. A., Graham, M. L., & Parrent, J. T. 2013, ATel, 5227
Valenti, S., Yuan, F., Taubenberger, S., et al. 2014, MNRAS, 437, 1519
Van Dyk, S. D., Li, W., Cenko, S. B., et al. 2011, ApJL, 741, L28
Van Dyk, S. D., Zheng, W., Brink, T. G., et al. 2018, ApJ, 860, 90
Van Dyk, S. D., Zheng, W., Fox, O. D., et al. 2014, AJ, 147, 37
Wellstein, S., & Langer, N. 1999, A&A, 350, 148
Wellstein, S., Langer, N., & Braun, H. 2001, A&A, 369, 939
Wheeler, J. C., Harkness, R. P., Clocchiatti, A., et al. 1994, ApJL, 436, L135
Williamson, M., Kerzendorf, W., & Modjaz, M. 2021, ApJ, 908, 150
Williamson, M., Modjaz, M., & Bianco, F. B. 2019, ApJL, 880, L22
Woosley, S. E., Heger, A., & Weaver, T. A. 2002, RvMP, 74, 1015
Woosley, S. E., Langer, N., & Weaver, T. A. 1995, ApJ, 448, 315
Yoon, S.-C. 2015, PASA, 32, e015
Zhang, J., Wang, X., Vinkó, J., et al. 2018, ApJ, 863, 109
Zhang, T., Wang, X., Zhang, T., et al. 2013, CBET, 3527, 1